October 2018

GEOMETRY, GROWTH AND PATTERN FORMATION IN THIN ELASTIC STRUCTURES

Salem Al-Mosleh

GEOMETRY, GROWTH AND PATTERN FORMATION IN THIN ELASTIC STRUCTURES

A Dissertation Presented

by

SALEM HMOUD AL MOSLEH

Submitted to the Graduate School of the
University of Massachusetts Amherst in partial fulfillment
of the requirements for the degree of

DOCTOR OF PHILOSOPHY

September 2018

Physics

GEOMETRY, GROWTH AND PATTERN FORMATION IN THIN ELASTIC STRUCTURES

A Dissertation Presented

by

SALEM HMOUD AL MOSLEH

Approved as to style and content by:

Christian Santangelo, Chair

Narayanan Menon, Member

Lorenzo Sorbo, Member

Gregory Grason, Member

Narayanan Menon, Department Chair
Physics

DEDICATION

To my parents.

To my wife for supporting me.

To my brothers and sister for encouraging me.

To Nancy and to Isam one of the best people I knew.

ACKNOWLEDGMENTS

Thanks to my advisor Christian Santangelo for being patient and teaching me how to be a good scientist. Thanks to group members Bryan Chen, Arthur Evans and Carlos Duque for valuable conversations. And thanks to Ajay Gopinathan for advising me on the growth and form project.

ABSTRACT

GEOMETRY, GROWTH AND PATTERN FORMATION IN THIN ELASTIC STRUCTURES

SEPTEMBER 2018

SALEM HMOUD AL MOSLEH

Ph.D., UNIVERSITY OF MASSACHUSETTS AMHERST

Directed by: Professor Christian Santangelo

Thin shells are abundant in nature and industry, from atomic to planetary scales. The mechanical behavior of a thin shell depends crucially on its geometry and embedding in 3 dimensions (3D). In fact, the behavior of extremely thin shells becomes scale independent and only depends on geometry. That is why the crumpling of graphene will have similarities to the crumpling of paper. In this thesis, we start by discussing the static behavior of thin shells, highlighting the role of asymptotic curves (curves with zero normal curvature) in determining the possible deformations and in controlling the folding patterns. In particular, we found that the presence of these curves on a surface can lead to more rigidity, and to continuously folding deformations. We then move to problems in growing thin shells, where the material properties change adiabatically with time. We derive here expressions for the quasi-static response of the shape to these changes. We focus in particular on changes in the target metric – analogous to the rest length of a spring. We derive an expression for the possible changes in the metric that are consistent with coordinate invariance, locality and dependent on geometry and applied forces. We apply this general framework, through

analytic calculations and simulations, to understanding how rod-like E. *coli* might be able to generate a stable elongating cylindrical shape. We show that coupling to curvature alone is generically linearly unstable and that additionally coupling to stress can lead to stably elongating cylindrical structures. Our approach can readily be extended to gain insights into the general classes of stable growth laws for different target geometries.

TABLE OF CONTENTS

LIST OF FIGURES

Figure **Page**

INTRODUCTION

Thin structures are found everywhere, in nature and industry, as well as in the lab. They are even found as one of the main tools of theoretical physics, paper. The mechanics of thin structures can be studied using the tools of differential geometry and Hooke's law. This gives it wide applicability to many problems on extremely different scales, from the planetary to atomic scales. We start our discussion by giving examples of the diverse problems studied within this framework, and highlighting connections with topics discussed later in this thesis.

On the planetary scale for example, Earth's lithosphere has been modeled as an elastic thin shell[1] and used in calculations of the perturbation to the shape of earth due to rotational motion [1]. Thin shell theory also appears in [2] to explain gravitational anomalies on the lunar surface, which are illustrated in Fig. (1).

You might wonder why elasticity – a field that is a few centuries old – is still active in physics today. In the past, a large deformation from a reference configuration was considered a mode of failure. For instance, a large deformation might result in the collapse of a bridge [3]. More recently [4], people have started to exploit instabilities and geometric nonlinearities, associated with large deformations that do not significantly stretch the material, as design tools. For example, in deployable satellites [5, 6], printable material [49, 50] and wrinkled electronics [7].

The field of extreme mechanics focuses on mechanical instabilities as a design tool rather than as modes of failure. An example of extreme mechanics in biology is the

[1]A thin shell is a thin elastic structure that is naturally curved. In other words, it's stress free configurations is curved.

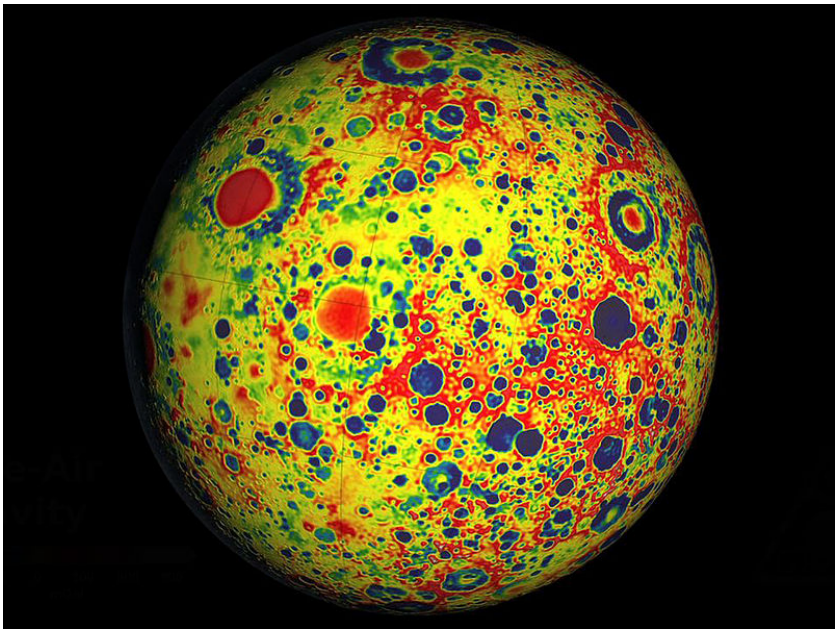

Figure 1. "This image shows the variations in the lunar gravity field as measured by NASA's Gravity Recovery and Interior Laboratory (GRAIL) during the primary mapping mission from March to May 2012". From Wikipedia

venus flytrap [8], which snaps shut when a fly is on its surface. This happens because of a mechanical instability that causes a snap-through transition, leading to fast motion [30]. In chapter (2), we discuss the mechanics of folding and snap-through on curved surfaces.

Biology provides many interesting applications of thin structure elasticity. For example, the blooming of lilies [9], rippling of leaves [10, 11] and even ripped plastic bags [12] have been described as elastic shells (or plates) with heterogeneous plastic deformations. Microscopic examples from biology include understanding the shape of viral capsids and fluctuations of red blood cells [13, 14, 15]. Understanding the mechanics of growing thin structures – such as the cell wall of E. *coli* [52, 51]– will be the topic of the last two chapters.

Finally, the atomic scale provides a limiting case of a shell with only a single atomic layer in thickness. The mechanical properties of graphene and its thermal

fluctuations have been studied in the context of thin shell elasticity [16, 17].

In chapter (2), we will study the low energy deformations of thin shells and describe them as nearly isometric deformations (defined as absence of stretching). We will see that curves where the Gaussian curvature changes sign, present a little paradox. When analyzed in the linear regime, there appears to be a smaller number of ways to deform these curves without stretching, which gives them the name "rigidifying" [18]. On the other hand, experiments have shown that it is possible to fold the surface continuously across these curves without significant stretching. So from that point of view these curves would be the opposite of rigidifying. In chapter (2), we give an explanation of this phenomena and solve for the folding isometries by considering geometric nonlinearities.

Chapter (3) gives a general framework for describing growth patterns in thin shells. Just like you can find the shape of a spring by knowing the forces acting on it and its preferred length, you can find the shape of a shell by knowing its preferred lengths and curvatures. In chapter (3), we find a growth law, describing the most general growth pattern that is consistent with certain symmetries. In chapter (4), we apply this framework to growth and form problems in rod-like E. *coli*.

In the next chapter, we will provide the necessary theory for understanding thin elastic shells. Some of this material will be repeated in later chapters when needed. You may skip the next chapter if you are familiar with differential geometry [43, 19] of surfaces and the energetics of elastic shells [18].

CHAPTER 1

ELASTICITY AND GEOMETRY

In this chapter we will review the basics of elasticity and the differential geometry of surfaces, laying the foundation for future chapters. We start with the geometry of piecewise smooth surfaces embedded in 3D Euclidean space (Sec. 1.1) and then briefly discuss how the theory of 3D elasticity reduces to a theory defined on 2D surfaces (Sec. 1.2).

1.1 Differential Geometry of Surfaces

The geometry of surfaces can be analyzed in terms of curves living on the surface. Therefore, we start our discussion with a lightning introduction to the geometry of curves. Refer to Figs. (3.1, 2.1) for illustration.

1.1.1 Geometry of Curves in 3D

Geometry is concerned with finding ways to measure and parametrize the shape of sets (we care about subsets of $\mathbb{R}^3$). A curve in 3D, can be parametrized by a single variable, for example, by the arc-length s. Its shape on the other hand, is given uniquely as a vector function of a single variable $\mathbf{X}(s)$, which gives the position in $\mathbb{R}^3$ of the points parametrized by s.

Of course, there are other measures of shape that are more physically relevant. For example, take a pen (if you still use pen and paper) and remove the outer plastic casing. You will be left with something that you can easily bend with the force of your hands. Notice that once forces are removed, the "natural" state of this pen is straight.

What geometric quantities describe the difference between bent and straight states? Derivatives of position with respect to arc-length along the curve can distinguish between such states.

The first derivative with respect to s is $\hat{t} \equiv \partial_s \mathbf{X}$, which has unit norm by definition when s is the arc-length. A pen wants $\hat{t}$ to be constant; deviations from that state are measured by the curvature vector $\kappa \equiv \partial_s \hat{t} = \kappa\ \hat{N}$. The unit vector $\hat{N}$ is normal to $\hat{t}$ and points toward the center of curvature[1]. Knowing $\hat{t}$ and $\hat{N}$, we can define a third vector, $\hat{b} \equiv \hat{t} \times \hat{N}$, which is perpendicular to both.

The last geometric measure of a curve that we will define is related to twisting. Twisting is an independent geometric measure from curvature, and can be defined through the derivative of $\hat{N}$. Specifically, $\partial_s \hat{N} = -\kappa\ \hat{t} + \tau\ \hat{b}$. To say this in words, when you move an infinitesimal amount in the direction $\hat{t}$, $\hat{N}$ changes in two ways. First, it rotates in the osculating plane due to the curvature. This first type of change happens for planar curves which are not twisting. The second type of deformation of $\hat{N}$ is out of the plane. In other words, this term describes how fast the $\hat{N}$ vector is twisting around $\hat{t}$ when you move forward.

Naturally, we can keep defining derivatives and geometric quantities. However, knowing κ and τ is usually enough to describe the energy cost of deformations. In addition, mathematically κ and τ are enough to determine the shape of the curve uniquely up to Euclidean motions.

1.1.2 Curves on Surfaces

We can use geometric measures of curves to describe the geometry of surfaces. First, we need to think about how to parametrize a surface. Locally, a surface is described by a vector function $\mathbf{X}(u^1, u^2)$, where u^1 and u^2 are arbitrary coordinates

[1]The subscript F in N_F is sometimes used to refer to the Frenet-Serret frame [19] described below.

parameterizing the surface — like θ, ϕ on a sphere. Even assuming that $\mathbf{u} \equiv (u^1, u^2)$ are arc-length parameters, does not fix them uniquely since we still need to specify the curves on the surface that they parametrize.

The first geometric quantity we will define is the metric. The metric makes easy the calculation of angles between curves, as well their lengths. Concretely, let $\gamma_1$andγ_2 be two curves on the surface defined by $\mathbf{u} = \mathbf{f}(t)$ and $\mathbf{u} = \mathbf{g}(t)$ respectively. Here $\mathbf{f} \equiv (f^1, f^2)$ and $\mathbf{g} \equiv (g^1, g^2)$, are functions of time parametrized by t. Assuming the two curves cross at $t = 0$, the dot product between the tangents of the two curves at $t = 0$ can be calculated using the chain rule as

$$\left(\partial_{u^i}\mathbf{X}\ \dot{f}^i\right) \cdot \left(\partial_{u^j}\mathbf{X}\ \dot{f}^j\right) = (\partial_i\mathbf{X} \cdot \partial_j\mathbf{X})\ \dot{f}^i\ \dot{g}^j \equiv g_{ij}(u^1, u^2)\ \dot{f}^i\ \dot{g}^j, \tag{1.1}$$

where the last equality defines the metric tensor on the surface. Note that we are using the Einstein summation convention, and the notation $\partial_i \equiv \partial_{u^i}$ and $df/dt \equiv \dot{f}$.

It can also be easily shown that the metric gives the length along the curve γ_1 as

$$L_{\gamma_1} = \int_0^t \sqrt{g_{ij}\ \dot{f}^i(t')\ \dot{f}^j(t')}dt' = s(t), \tag{1.2}$$

where $s(t)$ relates the arc length to the arbitrary parameter t. Furthermore, we can use the metric to define integrals over the area of the surface. Given a region $(u^1, u^2) \in \Omega$ in parameter space, the corresponding area element will be $dA = du^1 du^2 \sqrt{g}$, where g is the determinant of the metric. Note that, so far, everything said is independent of the definition of the coordinate grid (u^1, u^2) drawn on the surface.

As we will see in the next section, we will need to describe deformations of the surface as $\Delta\mathbf{X}(\mathbf{u}) \equiv \mathbf{Y}(\mathbf{u})$. Furthermore, it will be convenient to express this vector field on the surface using a basis that is natural to the surface. In particular, we will use two vectors tangent to the surface $\mathbf{e}_i \equiv \partial_i\mathbf{X}$ and a unit vector normal to the surface $\hat{n}$, which is to be contrasted with the Frenet normal $\hat{N}_F$. We can also define

the vectors $\mathbf{e}^i \equiv g^{ij}\ \mathbf{e}_j$, which are also tangent to the surface and where the inverse metric satisfies $g^{ij} \equiv (g_{ij})^{-1}$. With these definitions, we get the nice properties

$$\mathbf{e}_i \cdot \mathbf{e}_j = g_{ij} \quad \text{and} \quad \mathbf{e}^i \cdot \mathbf{e}_j = (\mathbf{e}_k \cdot \mathbf{e}_j)\ g^{ki} = g_{kj}\ g^{ki} = \delta^i_j, \tag{1.3}$$

where the last equality exploited the definition of the inverse metric and δ^i_j is the Kronecker delta.

Another important geometrical tool is needed when calculating derivatives of functions defined on a surface. Take for example a function $F(u^1, u^2) : \Omega \to \mathbb{R}$ which we wish to differentiate. The obvious thing to consider is the ordinary gradient $\partial_i F(u^1, u^2)$ with respect to the parametrization coordinates. This quantity obviously is not coordinate independent, but it changes in an obvious way under a coordinate transformation $\mathbf{y}(\mathbf{u})$, which can be derived using the chain rule.

The gradient $\partial_i F(u^1, u^2)$, while being dependent on the coordinate choice $\mathbf{u}$, can be used to define directional derivatives along curves. For example, along the curve γ_1 defined above, we have $dF/dt = \partial_i F\ \dot{u}^i$, which will give the same answer whether you chose the coordinates $\mathbf{u}$ or $\mathbf{y}(\mathbf{u})$. Coordinate invariance of a quantity is a sign that you're talking about a real quantity that you can build your physical theory around. You do not want to build a physical theory that depends on someone's choice of coordinates (Obviously!).

As we will see, we also need to take derivatives of vector fields $\mathbf{Y}(\mathbf{u}) : \Omega \to \mathbb{R}^3$. We will again calculate $\partial_i \mathbf{Y}$ and contract it with $\dot{u}^i$ to get a directional derivative along the surface. Furthermore, we can uncover more geometric quantities by breaking $\mathbf{Y}$ into its tangential and normal components, $\mathbf{Y} = Y^i\ \mathbf{e}_i + Y_n\ \hat{n}$. With this definition, we can directly compute

$$\partial_i \mathbf{Y} = \left(\partial_i Y^j + \Gamma^j_{ik} Y^k - b^j_i\ Y_n\right)\ \mathbf{e}_j + \left(Y^k\ b_{ik} + \partial_i Y_n\right)\ \hat{n}, \tag{1.4}$$

where we've defined the Christoffel symbols $\Gamma^j_{ik} \equiv \mathbf{e}^j \cdot \partial_i \mathbf{e}_k$ and the curvature tensor $b^j_i = g^{jk} b_{ki} \equiv \hat{n} \cdot \partial_i \mathbf{e}^j$. We will discuss the geometric meaning of the curvature tensor below. We can understand the geometric meaning of the Christoffel symbols, by focusing only on the tangential component of the field (which is the world of an ant living on the surface). If all you can measure were the components Y^i and $Y_n = 0$, then Eq. (1.4) reduces to

$$\mathbf{e}^j \, \partial_i \mathbf{Y} \equiv \nabla_i Y^j = \partial_i Y^j + \Gamma^j_{ik} Y^k. \tag{1.5}$$

This is the covariant derivative given in a general relativity class. It simply gives the ordinary derivative of the vector field $\mathbf{Y}$ when everything is restricted to the tangent plane of the surface.

We can also measure the curvature of the surface by looking at the curve γ_1. Assuming for simplicity that t is an arc-length parametrization, we can write the curvature of γ_1 as

$$\kappa \, \hat{N}_F = \partial s^2 \mathbf{X} = \left(\ddot{f}^i + \Gamma^i_{kj} \, \dot{f}^k \dot{f}^j \right) \mathbf{e}_i + \left(b_{ij} \, \dot{f}^i \dot{f}^j \right) \, \hat{n} \; = \; \kappa_g \, \hat{g} + \kappa_N \, \hat{n}. \tag{1.6}$$

Note that we split the curvature vector $\kappa \, \hat{N}_F$ – the definition of which does not depend on the surface – into a part that is normal to the surface called normal curvature κ_N, and a part that is tangent to the surface called geodesic curvature κ_g. The unit vector $\hat{g}$ is normal to the curve and tangent to the surface. As you can verify by squaring Eq. (1.6), κ_g only depends on the path through coordinate space $f^i(s)$, the metric and its derivatives. In other words if we deform the surface $\mathbf{X}(\mathbf{u})$ while preserving the value of the metric – an isometric deformation – κ_g will not change.

Finally Eq. (1.6) shows us the meaning of the curvature tensor: it is a bilinear form that helps calculate the normal curvature of curves. As with any symmetric matrix, you can diagonalize it and find its eigenvalues. Specifically,

$$b^i_j = \kappa_1\, v^i v_j + \kappa_2\, u^i u_j, \quad \text{where} \quad b^i_j\, v^j = \kappa_1\, v^i. \tag{1.7}$$

Even though this is different from the usual decomposition of the identity (since v^j and u^j are not orthonormal vectors, instead they satisfy the relation $g_{ij}u^i v^j = 0$), this still behaves as you would expect. For example, the trace – sum of diagonals – is given by $Tr[b] = \kappa_1 + \kappa_2 \equiv 2H$, were we defined the mean curvature H, which is a coordinate invariant function. The eigenvalues $\kappa_{1,2}$ are called principal curvatures and the directions u^i, v^j are called principal directions. Another very important measure of curvature is the Gaussian curvature given by $K \equiv \det(b^i_j) = \kappa_1\, \kappa_2$, which again is coordinate invariant.

In case you are wondering how on earth can we know if something is coordinate invariant, we will go back to the starting point and discuss how things change with different choices of coordinates. As we mentioned earlier, when you have a surface embedded in 3D, in order to start describing it and doing computations with it, you need to lay down a coordinate grid on it. The coordinates $(u^1, u^2) \in \Omega$ could come from an arbitrary set of curves that you draw on the surface. Once you have the coordinates you can describe the surface using the three function $\mathbf{X}(u^1, u^2)$. If you had used a different coordinate set $(y^1, y^2) \in \Omega'$, you would have gotten a different set of functions describing the surface. The two representations are related implicitly by $\mathbf{X}(u^1, u^2) = \mathbf{X}(u^1(\mathbf{y}), u^2(\mathbf{y}))$. Using this fundamental relation you can determine how quantities change with a coordinate transformation. For example

$$\mathbf{e}_i = \partial_{u^i}\mathbf{X} \to \partial_{y^{i'}}\mathbf{X} = \frac{\partial u^i}{\partial y^{i'}}\, \partial_{u^i}\mathbf{X}. \tag{1.8}$$

Things that transform according to $\Lambda_{i'}{}^{i} \equiv \frac{\partial u^i}{\partial y^{i'}}$ are called co-vectors. Whereas things that transform using $\Lambda^{i'}{}_{i} \equiv \frac{\partial y^{i'}}{\partial u^i}$, such as the components of a tangent vector $\dot{f}^i$, are called vectors. Notice that as a matrix, $\frac{\partial u^i}{\partial y^{i'}} = \left(\frac{\partial y^{i'}}{\partial u^i}\right)^{-1}$. With this setup, you can verify for yourself that H and K are coordinate invariants.

Finally, we mention the fundamental theory of surfaces, which states that knowing g_{ij} and b_{ij} is enough to completely determine the surface $\mathbf{X}$ up to rotations and translations. However, a surface will only exist if certain relations between g_{ij} and b_{ij} are satisfied. These conditions are called Gauss-Codazzi-Mainardi equations, we will give their explicit form in appendix (A). For now we will mention Gauss's Theorema Egregium, which states that the Gaussian curvature is completely determined by the metric and its derivatives, $\kappa_1\kappa_2 = K[g_{ij}]$. This equation has very important consequences on the behavior of thin elastic shells, as we will discuss shortly.

1.2 Elasticity of Thin Structures

We will derive the energy of a thin shell using an effective field theory approach. In other words, we will write down a set of possible terms consistent with symmetry, locality and analyticity. The energy of thin shells can also be derived starting from 3D elasticity as an asymptotic expansions in powers of thickness [18, 58].

It is convenient to first illustrate the idea for planar curves, then discuss how it generalizes to thin shells. We need an energy that is invariant under rotations, translations and reparametrization. For planar curves, curvature as a function of the arc-length parameter $\kappa(s)$ represents such an invariant quantity. In fact, $\kappa(s)$ completely determines the curve with arbitrary parametrization $\mathbf{X}(t)$ up to rotations, translations and reparametrization. In other words, all we need to do is write the linear energy density in terms of $\kappa(s)$ and its derivatives as $\mathcal{H}(\kappa(s), \kappa'(s), \cdots)$ and the symmetry assumptions will be satisfied. Since $\kappa(s)$ completely determines the shape of the curve, this represent a very general class of behaviors of planar curves.

To avoid writing down an infinite number of terms, we will write the energy density in the long wavelength (we will discuss what this means shortly) limit as

$$H[\kappa(s)] = \int ds \ \left[k_B \ (\kappa - \kappa_0)^2 + k_1 \ h \ \partial_s \kappa(s) + \cdots\right], \tag{1.9}$$

where $\kappa_0(s)$ is called the target (or reference) curvature and h is the thickness. Note that if we switch the direction of the parameter s, κ and κ_0 change sign, which explains the absence of the linear term. We have assumed here that the rod is inextensible so that the integration measure ds does not depend on the deformation. The constants k_B and k_1 are material parameters describing the rigidity of the rod to certain deformations.

As we just mentioned, Eq. (1.9) is truncated because the slope is small compared to the inverse length scale h^{-1} (long wavelength). By calculating the 3D elastic energy [58] of a thin rod, we find that h is the thickness of the rod and that $k_B, k_1 \propto h^4$. In other words, so long as the deformations are long compared to the thickness, the k_1 term can be safely ignored.

The last thing we will mention about the planar curves is regarding extensibility. Even though the shape of a curve is uniquely determined from knowing $\kappa(s)$, the energy is not. In other words, the same shape can have different energy costs depending on how it is reached from the reference configuration. For example, a straight line can be stretched in some places and compressed in others in such a way that the total length is unchanged. Mathematically speaking, there is a reference curve compared to which the energy can be defined. Parametrization invariance is not violated, but once a coordinate system is defined on the reference curve, it is fixed (referred to as material coordinates) on the deformed configuration.

A thin shell can be treated in the same way. Assume we have a reference metric $\bar{g}_{ij}$ and curvature tensor $\bar{b}_{ij}$, which together define the preferred lengths and curvatures of curves on the shell. If $\bar{g}_{ij}$ and $\bar{b}_{ij}$ are compatible and satisfy the Gauss-Codazzi-Mainardi equations, there will be a zero energy reference surface $\mathbf{X_0}$. As in the case of a rod, the existence of a reference surface means that the energy doesn't just depend on the shape, but also on the particular deformation vector $\mathbf{Y} \equiv \mathbf{X} - \mathbf{X}_0$.

Given the two tensors $\bar{g}_{ij}$ and $\bar{b}_{ij}$, we can write down the energy as an expansion

in powers of thickness

$$
\begin{aligned}
H\left[\mathbf{Y}; \bar{g}_{ij}, \bar{b}_{ij}\right] &= \int d^2u \, \sqrt{\bar{g}} \, \left[\mathcal{H}_{\text{stretch}} + \mathcal{H}_{\text{bend}}\right] \\
\mathcal{H}_{\text{stretch}} &= \frac{h}{8} \, A^{ijk\ell} \, \left(g_{ij} - \bar{g}_{ij}\right) \, \left(g_{k\ell} - \bar{g}_{k\ell}\right) \\
\mathcal{H}_{\text{bend}} &= \frac{h^3}{24} \, A^{ijk\ell} \, \left(b_{ij} - \bar{b}_{ij}\right) \, \left(b_{k\ell} - \bar{b}_{k\ell}\right),
\end{aligned} \tag{1.10}
$$

where $A^{ijk\ell} = \lambda \bar{g}^{ij} \, \bar{g}^{k\ell} + 2\mu \bar{g}^{ik} \, \bar{g}^{j\ell}$. Note that the cost of stretching scales as h, whereas bending scales as h^3. Thus, for very thin surfaces, bending costs very little energy compared to stretching. As a consequence, the low energy deformations of a shell will contain as little stretching as possible. Deformations that bend a surface without stretching it are called isometries, and they will be the subject of the next chapter.

Finally, as promised, we will discuss the significance of Gauss's theorema egregium to elastic shells. Since elastic shells deform in a nearly isometric way, the metric tensor g_{ij} will be very close to $\bar{g}_{ij}$. Gauss's theorem gives an identity between the product of the principal curvatures $K = \kappa_1 \, \kappa_2$ and the metric. Therefore, the product $K = \kappa_1 \kappa_2$ must remain nearly unchanged during the deformation. As a consequence, a cylinder ($K = 0$) can be flattened without stretching, but a spherical cap must be stretched or compressed to be turned into a planar domain.

CHAPTER 2

NONLINEAR MECHANICS OF RIGIDIFYING CURVES

2.1 Introduction

As a thin, elastic structure is deformed, it tends to flex without appreciably stretching. This is evident in a sheet of paper for example, which is soft to bending deformations but highly resistant to stretching [18]. Even under significant deformation, thin elastic structures tend to concentrate their stretching distortion into small regions of high strain surrounded by bent but relatively unstretched regions [20, 21, 22, 23, 24]. Because of this, isometries – deformations that deform a surface without stretching – play a privileged role in the mechanics of thin shells.

Roughly speaking, the more isometric deformations there are, the more ways you can deform a shell without stretching it. For example, the cross-sectional geometry of a thin, cylindrical shell can be deformed easily whereas a complete spherical shell cannot without introducing in-plane, and elastically costly, stretching. Indeed, a closed surface, such as a sphere, generically has no infinitesimal, smooth isometries [26]. Any deformations of a spherical shell must, therefore, balance stretching and bending.

Interestingly, Tenenblat [27] and, later, Audoly [28, 29], pointed out that in the vicinity of asymptotic curves– curves with zero normal curvature – the infinitesimal isometry equations are singular. As a result, there will be fewer smooth isometric degrees of freedom near those curves. Does that mean that these surfaces are more rigid in the zero thickness limit? If so, that would seem to be at odds with experiments described in Ref. [30], in which it was shown that a shell can be folded continu-

ously across an asymptotic curve without any stretching at all, while folding across a non-asymptotic curve would require traversing a stretching energy barrier.

In order to reconcile these two observations we need to find a (not necessarily smooth) family of nearly isometric deformations that connects the undeformed and folded states. And show that this deformation is energetically favored in the experimental conditions of [30]. This last point is discussed further in the conclusion in Sec. 2.4.

In this chapter, we seek to resolve this potential difficulty by accounting for the linearities in the elastic strain. Like the bending energy, these nonlinearities can also regularize the divergences in the linear isometries and naturally lead to the folded solution. We estimate the thickness range for which the correction due to the nonlinearities will be dominant over the bending energy considered in [28].

The chapter is organized as follows. In section 2.2, we give an overview of linear isometries and discuss their existence and properties. We derive the infinitesimal isometry equations and give explicit solutions to the particular case of a parabolic torus (Eq. 2.18), the behavior of the smooth and diverging solutions are explored near the rigidifying curves. In section 2.3, we show how the addition of the nonlinear terms in the isometry equation can regularize the divergences. We derive an approximate solution using the tools of boundary layer theory. The nonlinear solutions are then used to explain how folding across a rigidifying curve happens continuously and isometrically. We conclude in section 2.4.

2.2 Linear isometries for axisymmetric surfaces

2.2.1 Isometric deformations and mechanics of shells

We start this section by giving an overview of the relationship between isometric deformations and the mechanics of thin shells.

Starting with an undeformed shell, there are two related considerations for un-

derstanding the role of isometries in the mechanics of the shells. First, the allowed isometric deformations may be smooth or non-smooth. For example a sphere admits C^1 isometries with infinite bending cost. Of course in a real shell the sharp feature will be smoothed out, leading to finite energy cost related to the shell thickness in a nontrivial way [22]. A cylinder, on the other hand, admits many smooth isometries [25]. In principal, there can also be nonsmooth isometries with better continuity than C^1 [31, 32]. These isometries are far less costly even for small thickness.

Second, one can ask whether an isometry is connected to the undeformed state by a continuous one parameter family (or families) of isometries $\mathbf{X}(u^1, u^2, \epsilon)$. It was shown in the experiments in Ref. [30] that a shell can be continuously folded across an asymptotic curve without snapping, implying the existence of a family of isometric deformations connecting the undeformed and folded states.

For a smooth family $\mathbf{X}(u^1, u^2, \epsilon)$, we may define the infinitesmal isometry as $\mathbf{X}_1(u^1, u^2) \equiv \partial_\epsilon \mathbf{X}(\epsilon = 0)$. Equivalently, we may write

$$\mathbf{X}_0(u^1, u^2, \epsilon) \approx \mathbf{X}_0(u^1, u^2) + \epsilon\, \mathbf{X}_1(u^1, u^2). \tag{2.1}$$

If a smooth family of isometries $\mathbf{X}_0(u^1, u^2, \epsilon)$ fails ot exist, which implies the absence of infinitesimal isometries, the surface is said to be "rigid" in the sense defined in Ref. [26], in which it was proved that almost all simply connected closed surfaces are rigid.

2.2.2 General Linear Isometries and Self-Stresses

To be self-contained and to establish our notation, we start with a review of linear (or infinitesimal) isometries. We parametrize the shape of the shell in terms of the coordinates, $\mathbf{u} = (u^1, u^2)$, of its mid-surface (Fig. 2.1). We start with a reference surface, whose shape is given by the three-dimensional position of each point through

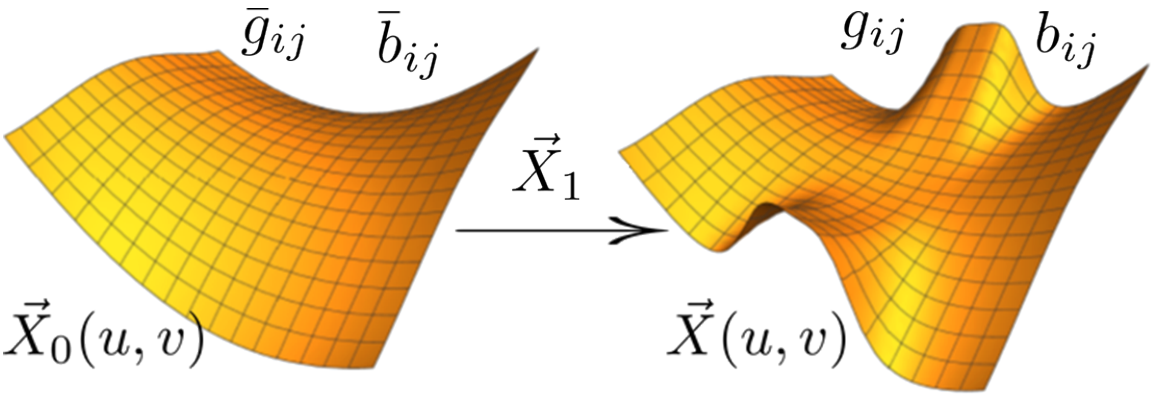

Figure 2.1. Displacement vector between two points on the mid-surface of a shell.

a vector function $\mathbf{X}_0(u^1, u^2)$. Therefore, the preferred distance between two points described by coordinates $u^i + du^i$ and u^i, for infinitesimal du^i, is given by the first fundamental form,

$$d\mathbf{X}_0^2 = \partial_i \mathbf{X}_0 \cdot \partial_j \mathbf{X}_0 \, du^i du^j \equiv \bar{g}_{ij} \, du^i du^j \tag{2.2}$$

where, in accordance with the Einstein summation convention, repeated indices are summed unless explicitly stated. The last equality defines the components of the (induced) reference metric tensor $\bar{g}_{ij}$, which encodes the equilibrium distances on the surface and must be symmetric and positive-definite. Similarly we define a deformed metric g_{ij} for the deformed surface $\mathbf{X}(u^1, u^2)$. Deformations for which $g_{ij} = \bar{g}_{ij}$, called isometries, satisfy

$$\partial_i \mathbf{X} \cdot \partial_i \mathbf{X} = \bar{g}_{ij}. \tag{2.3}$$

Consider a curve on the surface, with space curvature κ. The normal curvature is the projection of the curvature vector along the normal to the surface, and the

geodesic curvature is the projection along the tangent plane. This naturally leads to the relation

$$\kappa^2 = \kappa_N^2 + \kappa_g^2. \tag{2.4}$$

Curves with zero normal curvature are called asymptotic curves. Interestingly, the geodesic curvature does not change under isometric deformations, we exploit this fact in appendix A. For an arc length parametrization of the curve $u^i(s)$, the normal curvature is given by

$$\kappa_N = (\hat{\mathbf{n}} \cdot \partial_i \partial_j \mathbf{X}) \, \frac{du^i}{ds} \, \frac{du^j}{ds}, \tag{2.5}$$

where $\hat{\mathbf{n}}$ is the normal to the surface. We define the expression in the parentheses as the curvature tensor $b_{ij} \equiv \hat{\mathbf{n}} \cdot \partial_i \partial_j \mathbf{X}$.

For shells of very small thickness compared to curvature, we generically expect the deformations to be dominated by isometries [18]. This propensity is characterized by the Föppl-von Kàrmàn number, $\text{FvK} = BR^2/Y$, which measures the ratio of the bending stiffness B, characteristic length R and Young's modulus Y [33]. Typically, $\text{FvK} \propto R^2/t^2$ for shells of thickness t, showing that in-plane elasticity dominates over any bending energies [34, 35]. For large FvK, we study the deformations of a shell using the in-plane elastic energy [36]

$$E_s = \frac{1}{2} \int dA \; T^{ij} \left(\partial_i \mathbf{X} \cdot \partial_j \mathbf{X} - \bar{g}_{ij} \right), \tag{2.6}$$

where the stress T^{ij}, a symmetric tensor, is treated as a Lagrange multiplier to force the deformation to lie along an isometry. To this we add a bending energy

$$E_b = \frac{B}{2} \int dA \; \left(b_{ij} - \bar{b}_{ij} \right) \left(b^{ij} - \bar{b}^{ij} \right), \tag{2.7}$$

where $\bar{b}_{ij}$ measures the intrinsic curvature of the shell.

Next we derive equations governing the isometries of a shell's midsurface, $\mathbf{X}_0$. Consider a small deformation $\mathbf{X} = \mathbf{X}_0 + \mathbf{X}_1$ and a corresponding deformation of T^{ij} to $T^{ij} + T_1^{ij}$. Substituting this into the in-plane elastic energy and expanding to lowest order, we obtain

$$\begin{aligned} \delta E_s &= -\int dA \ \left(D_i T^{ij} \partial_j \mathbf{X}_0 \cdot \mathbf{X}_1 + T^{ij} \bar{b}_{ij} \hat{\mathbf{n}}_0 \cdot \mathbf{X}_1 \right) \\ &\quad + \int dA \ T_1^{ij} \left(\partial_i \mathbf{X}_0 \cdot \partial_j \mathbf{X}_1 \right) \\ &\quad + \oint d\ell \ T^{ij} \hat{\mathbf{k}}_i \partial_j \mathbf{X}_0, \end{aligned} \tag{2.8}$$

where D_i is the covariant derivative with respect to $\mathbf{X}_0$, $\hat{\mathbf{k}}$ is a vector tangent to the midsurface but normal to the boundary, and $d\ell$ is the integral over the boundary with respect to arc length.

Decomposing $\mathbf{X}_1$ into components tangent and normal to the surface,

$$\mathbf{X}_1 = A_n(u^1, u^2) \ \hat{\mathbf{N}} + A_i(u^1, u^2) \ \hat{\mathbf{e}}^i, \tag{2.9}$$

where $\hat{\mathbf{e}}^i$ are vectors tangent to the surface satisfying $\partial_i \mathbf{X}_0 \cdot \hat{\mathbf{e}}^j = \delta_i^j$ and δ_i^j is the Kronecker delta, we find that, to linear order, an isometry satisfies

$$-2 \ \bar{b}_{ij} A_n(u^1, u^2) + D_i A_j(u^1, u^2) + D_j A_i(u^1, u^2) = 0 \tag{2.10}$$

while the stress satisfies

$$D_i T^{ij} = 0, \qquad T^{ij} \bar{b}_{ij} = 0, \tag{2.11}$$

subject to the boundary condition $T^{ij} \hat{\mathbf{n}}_i = 0$. We call any $\mathbf{X}_1$ that satisfies Eq. (2.10) a *first-order*, or infinitesimal, isometry and any nonzero solution of Eqs. (2.11) a

self-stress. The relationship between self-stresses and isometries can be understood by index theory, but this is outside the scope of the current chapter [37].

When can we find a solution to the three equations in Eq. (2.10)? Naively, A_n appears algebraically in Eq. (2.10) and can be eliminated, leaving two equations in two unknowns. Since Eq. (2.10) is first-order, it appears that specifying the two in-plane deformations of a surface along a single curve is sufficient to determine the isometric deformation of the entire surface uniquely. However, the Gaussian curvature of the surface itself determines whether Eqs. (2.10) are elliptic or hyperbolic [28, 18]. Thus, any curve along which the Gaussian curvature changes sign, or alternatively one of the principal curvatures changes sign as it does in the torus (Fig. 2.2), changes the character of the isometry equations. Specifically, asymptotic curves (where $\kappa_N \equiv 0$) are the characteristics of Eq. (2.10). Because information propagates along these curves, unlike other curves, arbitrary boundary conditions cannot be specified on them. In other words, they have fewer infinitesimal isometric degrees of freedom. A consequence of the change from elliptic to hyperbolic in Eqs. (2.10) is that some linear isometries appear to diverge as they approach the curves of $\kappa_N, K = 0$ [28, 29].

Even when the Gaussian curvature does not vanish, a problem with Eqs. (2.10) can develop. For example, the horizon at the pseudosphere (Fig. 2.3) has one vanishing and one diverging principal curvature and cannot, consequently, be extended beyond its boundary despite K being constant.

2.2.3 Axisymmetric Surfaces and rigidifying curves

To demonstrate these features in simplest context, we specialize the linear isometry equations to axisymmetric surfaces. In that case, the embedding, $\mathbf{X}_0$, can be expressed as

$$\mathbf{X}_0(s,\theta) = s\ \hat{s}(\theta) + h(s)\ \hat{z}, \tag{2.12}$$

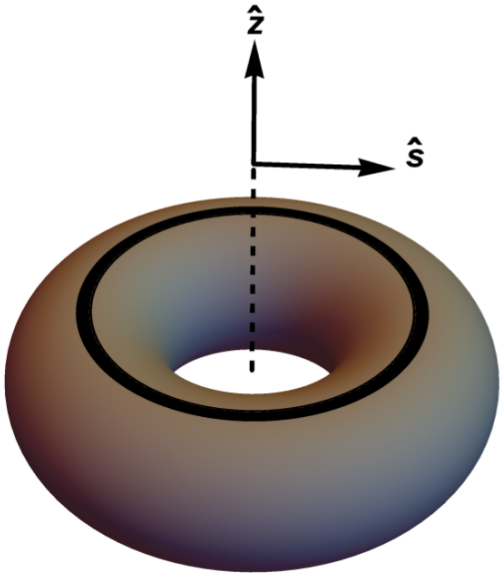

Figure 2.2. Torus with a curve of $\kappa_N = 0$ shown in black.

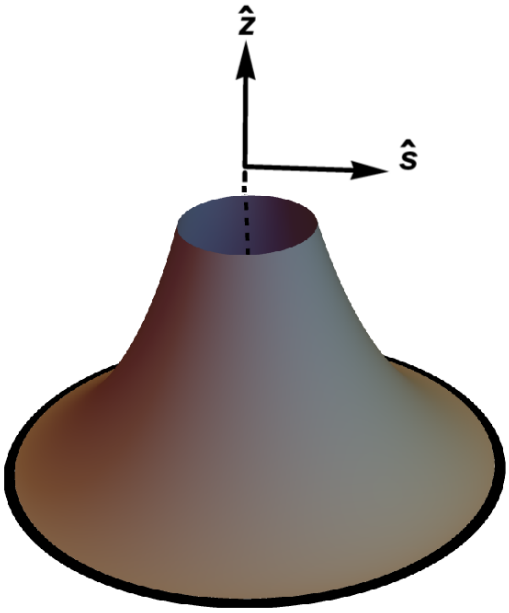

Figure 2.3. Pseudosphere with the curve of $\kappa_N = 0$ shown in black.

where s is the radial distance from the $z-$axis, $\hat{s}$ is the unit vector pointing in the radial direction, and $h(s)$ is the vertical height of the surface. The tangent vectors are $\partial_\theta \mathbf{X}_0 = s\ \hat{\theta}$ and $\partial_s \mathbf{X}_0 = \hat{s} + h'(s)\ \hat{z}$, where the prime indicates a derivative with respect to s. The first and second fundamental forms are

$$\bar{g}_{ij} = \begin{pmatrix} 1 + h'(s)^2 & 0 \\ 0 & s^2 \end{pmatrix} \tag{2.13}$$

and

$$\bar{b}_{ij} = \frac{1}{\sqrt{1 + h'(s)^2}} \begin{pmatrix} h''(s) & 0 \\ 0 & s\ h'(s) \end{pmatrix}. \tag{2.14}$$

The normal curvature along the curves of constant s vanishes when $h'(s) = 0$; these are precisely the rigidifying curves.

An arbitrary displacement of the surface can be written as

$$\mathbf{X}_1(s,\theta) = A_s(s,\theta)\hat{s}(\theta) + A_\theta(s,\theta)\hat{\theta}(\theta) + A_z(s,\theta)\hat{z} \tag{2.15}$$

in terms of the basis $(\hat{s}, \hat{\theta}, \hat{z})$. We can exploit the axisymmetry of the isometry equations by expressing them in terms of the Fourier transforms of the functions $A_i(s,\theta)$,

$$A_i(s,\theta) = \sum_m\ \tilde{A}_i(s,m)\ e^{im\theta} \tag{2.16}$$

where m is an integer. After some algebra, these three equations can be combined into a single equation for each mode m for $\tilde{A}$,

$$\tilde{A}_z''(s) + \frac{h''(s)}{h'(s)}\ \tilde{A}_z'(s) - \frac{m^2\ h''(s)}{s\ h'(s)}\ \tilde{A}_z(s) = 0. \tag{2.17}$$

This second-order differential equation has two analytic solutions as long as $h'(s) \neq 0$. If there is a singularity, $h'(s^*) = 0$ for some $s = s^*$, it will be regular if $h'(s) \sim (s - s^*)$ as s approaches s^*.

We illustrate the behavior of the isometries near the curve $h'(s^*) = 0$, by considering the "parabolic torus" near the rigidifying curve described by

$$h(s) = \frac{1}{2\,a}\,(s - R)^2. \tag{2.18}$$

The surface of Eq. (2.18) can be thought of as an approximation of more general axisymmetric surfaces near a rigidifying curve at $s = s^*$. Since $h'(R) = 0$ with $h''(R) \neq 0$, Eq. (2.17) has a regular singularity at $s = R$ and, indeed, the surface described by $h(s)$ has a circle of zero normal curvature along $s = R$. In dimensionless variables, the linear isometry equation becomes

$$\partial_u^2 Y_z(u) + \frac{1}{u}\partial_u Y_z(u) - \frac{m^2}{u(u+1)} Y_z(u) = 0, \tag{2.19}$$

where $u \equiv (s - R)/R$ and $\tilde{A}_z(u) \equiv R\, Y_z(u)$. The solutions have the form

$$Y_{zm} = A_m\ {}_2F_1(-m, m; 1; -u) + B_m\ \log|u|\ {}_2F_1(-m, m; 1; -u) + B_m\ {}_2G_1(-m, m; 1; -u), \tag{2.20}$$

and

$${}_2G_1(\alpha, \beta; 1; -u) \equiv \sum_{r=1}^{\infty} \left[\frac{\Gamma(\alpha + r)\,\Gamma(\beta + r)}{\Gamma(\alpha)\Gamma(\beta)(r!)^2} \sum_{k=0}^{r-1} \Big(\frac{1}{\alpha + k} + \frac{1}{\beta + k} + \frac{2}{1 + k} \Big)\ (-u)^r \right], \tag{2.21}$$

where A_m and B_m, are constants, ${}_2F_1(a, b; c; z)$ is a hypergeometric function, and we have defined the analytic function ${}_2G_1(-m, m; 1; -u)$. The functions $A_{zm}(u)$, $A_{sm}(u)$

and $A_{\theta m}(u)$, for $m > 1$, can be found from $Y_{zm}(u)$ and the isometry equations. Figs (2.4 -2.7) illustrate these solutions for the parabolic torus of Eq. (2.18).

Thus, Eq. (2.20) has one solution that diverges logarithmically as $u \to 0$ for each mode m. The asymptotic behavior of the solutions for $u \ll 1$ is

$$Y_{zm}(u) = A_m + B_m \ \log|u| + O(u \log u). \tag{2.22}$$

Taking the inverse Fourier transform we can rewrite this limit as

$$Y_z(u,\theta) = A(\theta) + B(\theta) \ \log|u| + O(u \log u) \tag{2.23}$$

where $A(\theta)$ and $B(\theta)$ are arbitrary functions of θ. Any axisymmetric surfaces satisfying $h(s) \propto (s - s^*) + O\left((s - s^*)^2\right)$ will have the same leading behavior given in Eq. (2.23). In the next section, this form will be convenient for asymptotic matching to the nonlinear solution in the vicinity of the rigidifying curve. The solutions to A_θ and A_s corresponding to the diverging solution are also non-analytic at $u = 0$, but they both vanish as $O(u \ \log u)$ as $u \to 0$.

Naive considerations would suggest that we require $B_m = 0$ to avoid the divergences that occur in the isometry. However, the approximation of linear elasticity also breaks down near the rigidifying curve. As we will see in the next section, when we include nonlinear terms in our analysis, the divergence of the isometry is regularized.

2.3 Nonlinear mechanics of rigidifying curves

Though we may be tempted to exclude the diverging solutions, only the vicinity of the rigidifying curves becomes rapidly varying and large. Thus, two of our assumptions become invalid near the rigidifying curves: the bending energy may not be neglected and geometrical nonlinearities in the strain are no longer negligible. For sufficiently thin surfaces (see Eq. 2.28), the bending energy can always be made

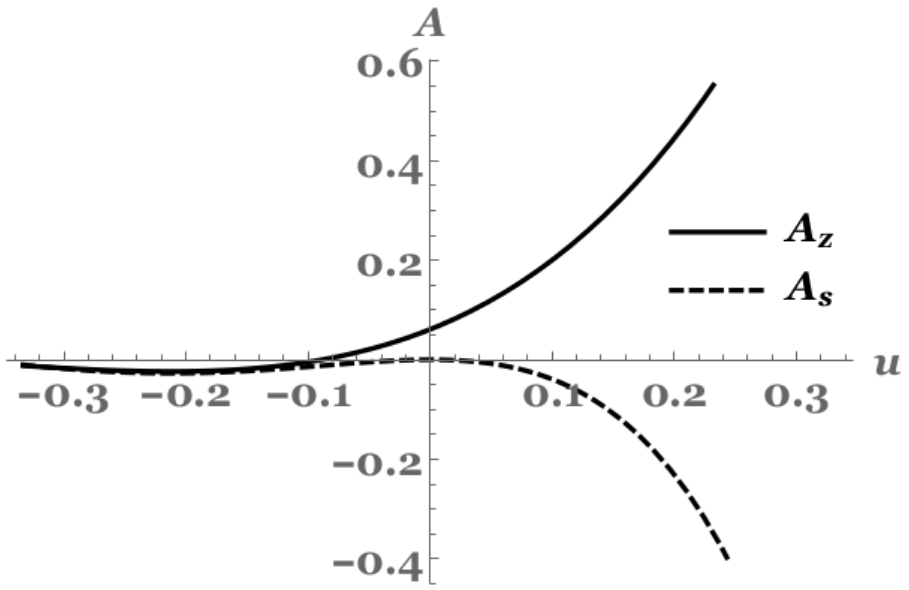

Figure 2.4. Smooth isometric deformations of the parabolic torus, normalized so that A(s = R + a) = 1 and m = 4. A_z and A_s represent displacements of the initial surface, rather than absolute positions.

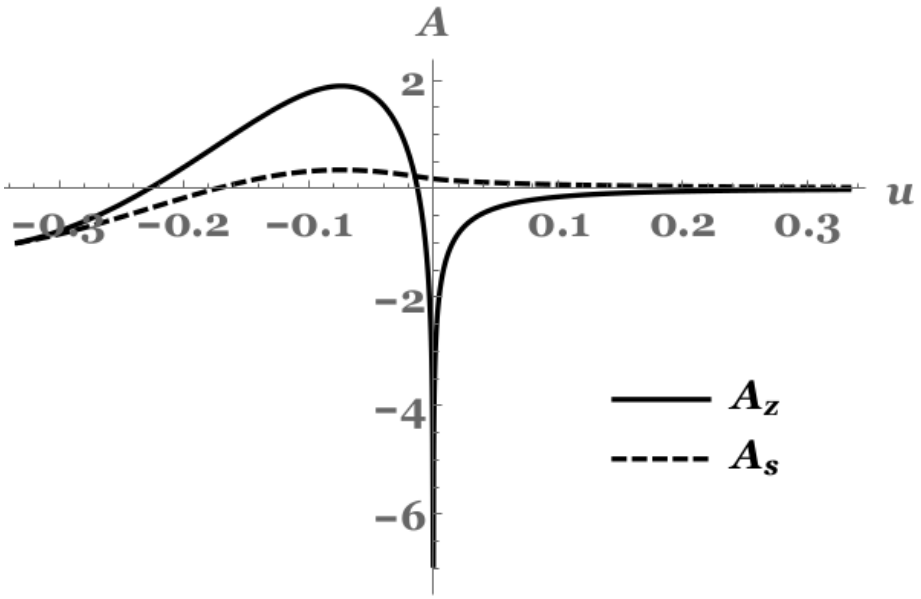

Figure 2.5. Diverging isometric deformations of the parabolic torus, normalized so that A(s = R - a) = 1 and m = 4. Notice that the displacement in the z-direction behaves as $A_z \sim \log u$ as $u \to 0$

Figure 2.6. Surface deformed by smooth linear isometry.

Figure 2.7. Surface deformed by diverging linear isometry.

smaller than the nonlinear strain terms, therefore we will consider the effect of the unavoidable nonlinearities.

The full nonlinear isometry equations are, unfortunately, complicated. They read

$$2\partial_s A_s + 2h'(s)\partial_s A_z + (\partial_s A_s)^2 + (\partial_s A_\theta)^2 + (\partial_s A_z)^2 = 0, \tag{2.24}$$

$$2s\left(\partial_\theta A_\theta + A_s\right) + \left(\partial_\theta A_s - A_\theta\right)^2 + \left(\partial_\theta A_\theta + A_s\right)^2 + \left(\partial_\theta A_z\right)^2 = 0, \text{ and} \tag{2.25}$$

$$s\partial_s A_\theta + \partial_\theta A_s - A_\theta + h'(s)\partial_\theta A_z + \left(\partial_\theta A_s - A_\theta\right)\partial_s A_s + \left(\partial_\theta A_\theta + A_s\right)\partial_s A_\theta + \left(\partial_\theta A_z\right)\left(\partial_s A_z\right) = 0. \tag{2.26}$$

As in section 2.2.3, we assume $h(u) \approx (s-R)^2/(2a)$ and $u = (s-R)/R$ as $s \sim R$.

If we substitute in the linear solution, we note that $A_\theta \sim u \log u$ and $A_s \sim u \log u$, suggesting that the terms nonlinear in A_s and A_θ can be ignored. This approximation can be justified post-hoc. Within this approximation, we set $A_z(s,\theta) = R^2 Y_z(u,\theta)/(2a)$ and use the linearized forms of Eqs. (2.24) and (2.25) to eliminate A_s and A_θ. Thus, we obtain a single equation for Y_z,

$$\begin{aligned} 0 \;=\; & 2\,(1+u)\,\partial_u Y_z + 2\,u\,(1+u)\partial_u^2 Y_z + 2\,\partial_\theta^2 Y_z \\ & - \frac{\left[\partial_\theta Y_z - (1+u)\,\partial_\theta \partial_u Y_z\right]^2}{(u+1)^2} + \\ & \left[\partial_\theta^2 Y_z + (1+u)\,(2u + \partial_u Y_z)\right]\partial_u^2 Y_z. \end{aligned} \tag{2.27}$$

Eq. (2.27) can be solved numerically (the results are shown in Appendix B). Here, we will pursue an analytic approach to obtaining approximate solutions. There are three regimes. The linear solution is valid when $u \gg |Y_z(u \sim \frac{a}{R})|^{1/2}$. Within the layer $u \lesssim |Y_z(u \sim \frac{a}{R})|^{1/2}$, the nonlinearities become important and the linear solution is no longer valid. For the nonlinearities to become important before the bending energy modifies the solution, the width of this layer (λ_N) must be bigger than the width of

the layer that would result from bending energy regularization $\lambda_B \sim (t\ R\ a)^{1/3}$ [29]. Therefore, our analysis is valid when

$$\lambda_B \ll \lambda_N \quad \Longrightarrow \quad t \ll \frac{R^2\ |Y_z(u \sim \frac{a}{R})|^{3/2}}{a}. \tag{2.28}$$

When this condition is met we can obtain a finite solution to Eq. (2.27) in powers of u near the rigidifying curve (Appendix B). This shows that the nonlinear terms are sufficient to regularize the divergences of the nonlinear theory. This is the "inner solution" in the language of boundary layer theory. In the intermediate regime, $|Y_z(u \sim \frac{a}{R})|^{1/2} \ll u \ll 1$, we may obtain a better approximation by considering how large the various terms in the nonlinear equation become as we approach the rigidifying curve when substituting the linear solution into Eq. (2.27). The most divergent term is proportional to $\partial_u Y_z\ \partial_u^2 Y_z$, which behaves as $\sim 1/u^3$ for small u, whereas all the other nonlinear terms diverge as $\sim u^{-2}$ or slower. On the other hand, the first two linear terms in the equation are $O(u^{-1})$ and the linear term $\partial_\theta^2 Y_z$ only grows as $\log u$. Taken together, this suggests that Eq. (2.27) has a regime, $|Y_z(u \sim \frac{a}{R})|^{1/2} \ll u \ll 1$, where all the nonlinear terms except the last term can be treated as a perturbation. This argument does not work when the coefficient of the $\log u$ term vanishes at some value of θ. We will treat these regions separately and unless otherwise stated we will assume that the coefficient of the $\log u$ solution is greater than zero.

The resulting reduced equation can be written in the form

$$\partial_u \left[u \partial_u Y_z + \frac{1}{4} (\partial_u Y_z)^2 \right] = 0, \tag{2.29}$$

and solved by

$$\partial_u Y_z(u, \theta) = -2\ u \pm \sqrt{4\ u^2 + \gamma_\pm(\theta)}, \tag{2.30}$$

where $\gamma(\theta)$ is a constant of integration. We can now solve for the z-component of the displacement by integrating (2.30) to find

$$Y_{z\pm}(u) = \delta_\pm(\theta) - u^2 \pm \frac{u}{2}\sqrt{4\ u^2 + \gamma_\pm(\theta)} + \frac{\gamma_\pm(\theta)}{8}\log\left(\frac{\pm 2\ u + \sqrt{4\ u^2 + \gamma_\pm(\theta)}}{\sqrt{\gamma_\pm(\theta)}}\right)^2 \quad (2.31)$$

where $\delta_\pm(\theta)$ is another integration constant. Note that there are two branches of solution, shown in Fig. (2.8), with opposite signs of the normal curvature $\kappa_N \sim \pm\sqrt{\gamma_\pm}$. This is what we would expect (see [38]) from the relation $\kappa_N = \pm\sqrt{\kappa^2 - \kappa_g^2} \sim \pm\sqrt{\delta\kappa}$ (see Eq. (2.4) and appendix A for more details).

Note that $Y_{z\pm}$ remains finite as $u \to 0$, quite unlike it does in the case of infinitesimal isometries. In the limit $u/|\gamma_\pm|^{1/2} \ll 1$, this solution behaves as the regular series

$$Y_{z\pm} = \delta_\pm(\theta) \pm \sqrt{\gamma_\pm(\theta)} - u^2 \pm \frac{2\ u^3}{3\sqrt{\gamma_\pm}}, \quad (2.32)$$

This series can be matched to a series expansion solution of Eq. (2.27) near the rigidifying curve. Notice that the solution does not make sense unless $\gamma_\pm > 0$. In light of the relation $\kappa_N \sim \pm\sqrt{\delta\kappa} \sim \pm\sqrt{\gamma_\pm}$, this requirement is equivalent to the requirement that $\delta\kappa > 0$, or that $\kappa > \kappa_g$ within our approximation. More generally it can be shown that the full (no approximations) isometry equations are not well behaved when κ_N changes sign (see appendix A).

The limit $u/|\gamma_\pm|^{1/2} \gg 1$ (for $u > 0$), on the other hand, yields

$$Y_{z+} = F_+(\theta) + \frac{\gamma_+(\theta)}{4}\ \log u \quad (2.33)$$

$$Y_{z-} = -2u^2 + F_-(\theta) - \frac{1}{4}\gamma_-(\theta)\ \log u \quad (2.34)$$

$$F_\pm = \frac{1}{8}\left(\pm\gamma_\pm(\theta) + \gamma_\pm(\theta)\ \log\left(\frac{16}{\gamma_\pm(\theta)}\right) + 8\ \delta_\pm(\theta)\right). \quad (2.35)$$

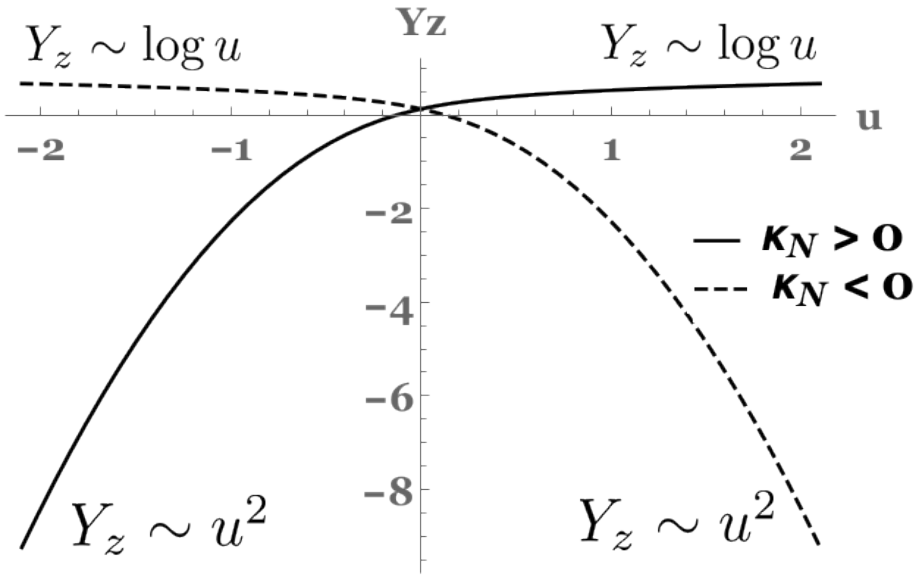

Figure 2.8. The two inner solutions obtained from equation (2.3) with $\delta_\pm = 0.2\ \cos(2\ \theta)$ and $\gamma_\pm = 0.6 + 0.3\ \cos(2\ \theta)$, evaluated at $\theta = \pi/7$. The two solutions have opposite signs of normal curvature, which is required for existence of folding isometries [38, 30].

The form of this solution can be matched to the infinitesimal isometry far from the rigidying curve. Notice that it is only possible to match one of the solutions (Y_{z+}) to the region $u \gg \epsilon^{1/2} > 0$. The $-2u^2$ behavior of Y_{z-} corresponds to the deformation $h(s) \to -h(s)$, which is a reflection of the undeformed surface about the z-axis.

Similarly, if $u < 0$, the limit $|u|/|\gamma_\pm|^{1/2} \gg 1$ yields

$$Y_{z+} = -2u^2 + G_+(\theta) - \frac{1}{4}\gamma_-(\theta)\ \log u \tag{2.36}$$

$$Y_{z-} = G_-(\theta) + \frac{\gamma_+(\theta)}{4}\ \log u \tag{2.37}$$

$$G_\pm = \frac{1}{8}\left(\mp\gamma_\pm(\theta) + \gamma_\pm(\theta)\ \log\left(\frac{16}{\gamma_\pm(\theta)}\right) + 8\ \delta_\pm(\theta)\right). \tag{2.38}$$

We again find that only one of the solutions can match the linear behavior on the $u < 0$ side. Interestingly, in this case it is Y_{z-} that matches the linear solution.

Thus, each of the smooth solutions match the linear isometries only on one side

of the rigidifying curve. On the other side, the smooth isometry approximates the reflection of the original parabolic torus about the z-axis. Take for example A_{z+}, the z-component of the isometry corresponding to Y_{z+}. In the limit $\gamma_+ \to 0$ and $\delta_+ \to 0$ it is approximately equal to

$$A_{z+} = \begin{cases} \frac{(s-R)^2}{2\,a} & s > R \\ \frac{-(s-R)^2}{2\,a} & s < R, \end{cases} \tag{2.39}$$

which is the original parabolic torus with the region $s < R$ reflected along the z-axis. While being isometric to the original surface, it is not connected to it through a small displacement. Thus there will be an energy barrier preventing the solutions Y_{z+} and Y_{z-} from being realized starting from the undeformed torus.

To construct a solution that is connected to the parabolic torus through a small displacement, we need to glue A_{z+} in the region $s > R$ with A_{z-} on $s < R$. This results in an isometry that is not smooth on the curve s = R, on one side of the curve, A_{z+} has a positive normal curvature, while the opposite side has a negative normal curvature. This is what you would expect when two surfaces are joined isometrically along a fold (see Refs [38], [39] and [30]).

Whether this actually happens in practice will depend on the energetics of stretching and bending. The folded solution can be made energetically favorable if the surface is creased (made thinner) at the curve $s = R$ as was done experimentally in [30]. In the remainder of this section, we will construct explicitly the global isometric solution by gluing together the partial solutions in the various regimes.

We have already seen that in the regime $u \ll 1$, the linear solution takes the form of Eq. (2.23). There is an overlap between the regions of validity of both these approximations, namely $\delta_\pm^{1/2} \lesssim u \lesssim 1$, so we may match them to obtain [41]

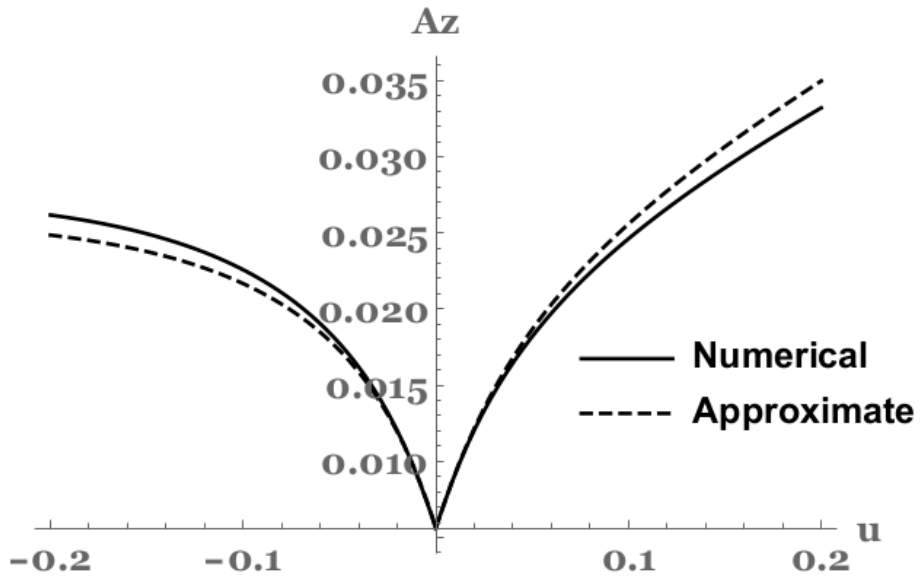

Figure 2.9. Comparing the numerical solutions of Eq. (2.27) to the matched approximation. Here a = 1, R = 3, $\delta_+ = 0.002\ \cos(2\,\theta)$ and $\gamma_\pm = 0.006 + 0.003\ \cos(2\,\theta)$

$$A(\theta) = \frac{R}{2\,a} F_+(\theta), \quad B(\theta) = \frac{R}{8\,a}\,\gamma_+(\theta),\ u > 0, \tag{2.40}$$

$$A(\theta) = \frac{R}{2\,a} G_-(\theta), \quad B(\theta) = \frac{R}{8\,a}\,\gamma_-(\theta),\ u < 0. \tag{2.41}$$

Therefore the two assumptions that we made, $B(\theta) \neq 0$ and $\gamma_\pm > 0$, are consistent. Fig. 2.9 shows the agreement between the matched inner and linear approximations [1] and the numerical solution of Eq. (2.27).

Consider the setup shown in Fig. 2.10. We attach a frame of a given shape to the rigidifying curve. Since the curve has only two isometric degrees of freedom, we need only specify $A_z(\theta)$ and $A_s(\theta)$ on the curve and $A_\theta(\theta)$ will be determined. Specifically

[1]Remember that the linear solutions were found under periodic boundary conditions in θ and, while we may chose $\gamma_\pm$ and $\delta_\pm$ to be periodic, this will only ensure that A_z and A_s are periodic, while A_θ will not be. Indeed, our simulations have shown that a closed torus has only rigid isometries. This is not a problem for our matching solutions as long as we think of the parabolic torus as open with angular size $\Delta\theta < 2\pi$

$$A_z(s=R,\theta) = \frac{R^2\ \delta_\pm(\theta)}{2\ a} \tag{2.42}$$

$$A_s(s=R,\theta) = \frac{R^2\ \tau_\pm(\theta)}{2\ a}, \tag{2.43}$$

where $\tau_\pm$ is determined by $\gamma_\pm$ using the series solution of the isometry equation (2.26), and where we neglected the nonlinearities in A_θ and A_s. To leading order in $|\delta_\pm|$ and up to rigid xy-translations, we have

$$\tau_\pm(\theta) = \frac{a}{R}\ \mathrm{Re}\left[i\ e^{i\,t}\int_0^t e^{-i\,\sigma}\ \gamma_\pm(\sigma)\ d\sigma\right], \tag{2.44}$$

This choice fixes $A_s(u=0,\theta=0)=0$.

Interestingly there is no way to distinguish whether we are in the $\kappa_N > 0$ branch or the $\kappa_N < 0$ branch just by knowing the shape of the deformation at $s = R$. Either isometry can be attached to a given boundary condition and can be continuously reached from the undeformed torus (but not smoothly, because of the $\gamma_\pm^{1/2}$ in the solutions). This is consistent with the results in Refs [30] and [39].

Finally, notice that the constraint $\gamma_\pm > 0$ can be expressed as a constraint on the s-displacement of the rigidifying curve or, equivalently, on the shape of the boundary curve. Consider the curves perpendicular to the rigidifying curve. On an undeformed (parabolic) torus they are (parabolas) circles satisfying $\theta =$ constant, and with tangents at $u = 0$ pointing toward the center of the torus in the xy-plane. After isometric deformation, the tangents are still perpendicular to the rigidifying curve (Fig. 2.10), but since $\partial_u A_z > 0$ when $u > 0$ and $\partial_u A_z < 0$ when $u < 0$, these curves will be pointing strictly above the xy-plane. This is another way to express the requirement $\gamma > 0$.

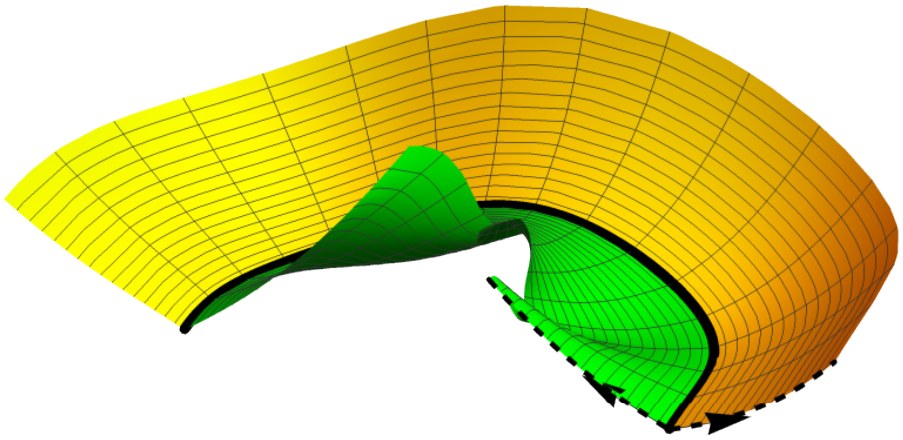

Figure 2.10. The nonlinear isometries corresponding to $\delta_{\pm} = 0.1\ \cos(4\ \theta)$ and $\gamma_{\pm} = 0.2 + 0.15\ \cos(4\ \theta)$ joined continuously at u = 0. The region $u < 0$ represents the surface deformed by the isometry corresponding to Y_{z-} which satisfies $\kappa_N < 0$. The $u > 0$ region in green (shaded), corresponds to Y_{z-} and satisfies $\kappa_N > 0$. The dashed curves satisfy $\theta = 0$, and the arrows are their tangents at u = 0. As explained in the text the arrows are perpendicular to the rigidifying curve and must stay strictly above the xy-plane because of the requirement $\gamma_{\pm} > 0$.

2.4 Conclusion

We showed in section 2.2.3 that some of the infinitesimal isometries of surfaces diverge near a rigidifying curve. Taken at face value this seems to indicate a reduction in the number of isometries of the surface near these curves. Indeed it can be shown using geometric arguments (see appendix A and [18]) that rigidifying curves have constant curvature κ under linear isometries.

On the other hand, the experiments in [30] show that folding along curves with $\kappa_N = 0$ can happen continuously without a stretching energy barrier. We have shown, in section 2.3, how the presence of nonlinear terms in the isometry equations reconciles these two observations. The argument for the rigidity of the $\kappa_N = 0$ curves relies on the assumption that an expansion of the form $\mathbf{X}(\epsilon) = \mathbf{X}_0 + \epsilon\ \mathbf{X}_1 + \cdots$ exists, where ϵ parametrizes the isometries. However we have shown, using series and boundary layer approximations of the full isometry equations that the solution cannot be analytic in

ϵ. In the full nonlinear solution, the normal curvature can be different from zero after deformation.

Moreover, we found pairs of solutions having opposite signs of normal curvature across a rigidifying curve. These correspond to continuous solutions across $\kappa_N = 0$ curves.

Further work must be done to understand the energetics of these "folded" isometries and why they seem to be realized in experiment instead of the smooth isometries of Fig. 2.8. Since the smooth isometries have an unavoidably large component proportional to u^2 whereas the folded on can have arbitrarily small displacements, there will be a range in parameter space where the folded solutions-with a suitably smoothed fold- is favorable energetically. However it is likely that the smooth solutions are not realized because of a lack of a low energy paths in deformation space leading to them starting from the reference surface, even if their energy is lower. The folded solutions on the other hand can start infinitesimally close to the starting surface and be varied continuously.

CHAPTER 3

GROWTH OF FORM IN THIN ELASTIC STRUCTURES

3.1 Introduction

How physical processes establish the growth and form of biological structures was considered by D'Arcy Thomson almost a century ago [44]. Since then, there has been much progress explaining the different growth driven morphologies that appear in the natural world. These include understanding that the rippled edges of leaves [45], the ruffled petals of blooming lilies and other flowers [9, 47], and even the convolutions of the brain cortex may be driven by differences in growth rate between spatially distinct regions [46]. It is well known that heterogeneous insertion and deletion of material can lead to geometric frustration and shape change in synthetic tissues [48, 49, 50]. Yet one hundred years after D'Arcy Thomson's seminal work, there are still challenges and open problems. One such challenge is that of determining the connection between the dynamical growth law —where a tissue chooses to grow —and both the shape and stability of those tissues.

This raises the question of how growth laws are regulated in nature to ensure stable growth. Feedback is a commonly used mechanism in biology for ensuring stability, but it is not clear to what or how the growth laws need to be coupled, to ensure the robust growth of a stable structure. A particular example of this issue is the question of shape regulation in rod-like *E. coli*, which is still an open problem [51, 52]. Though the components of the molecular machinery responsible for cell wall growth and regulation have been identified [53], precisely how the nm-scale components within this network interact to produce a robust shape at the μm-scale is

not completely understood. Feedback between cell wall insertion rate and curvature, which was shown to be present in *E. coli* [54], can in principal lead to stable cylindrical shapes. However, as demonstrated in Refs. [55] and [56], stress also affects cell wall insertion rate and can lead to growth which is different from what would be expected from a purely geometric coupling.

In this chapter, we step back from the details of the growth process and consider a general framework for describing the growth of thin elastic structures that allows us to study stability. We assume that throughout the growth process, the material retains uniform thickness and Young's modulus. That is to say, it is still made of the same stuff, there is just more of it in some places and less in others. Mathematically, this growth process can be described as a change in the reference metric of the shell or, alternatively, as the change in the local equilibrium lengths between points along the surface [7]. There are, of course, an infinity of ways that the reference metric could change in time.

Here we consider regulating the growth by coupling the growth laws to purely local properties of the shape, such as the local curvature and stress. It is then possible to use considerations of symmetry and locality to make a curvature expansion and reduce the growth laws to only few effective parameters. Our approach thus allows us to study the relationship between geometry and stress in determining the morphological stability of growing structures. Partially motivated by E. coli and partially for concreteness, we use our formalism to address the linear stability of elongating, cylindrical shapes as an example. Nevertheless, we develop principles that can be applied to morphology selection and stability in biological systems more generally.

This chapter is organized as follows. In Sec. (II), we give a short overview of the required differential geometry. In Sec. (III) we consider the energetics of thin elastic shells, using the Helfrich Hamiltonian. In section (IV) we describe the growth process, and show how symmetry can help us organize the different possible growth laws. Sec.

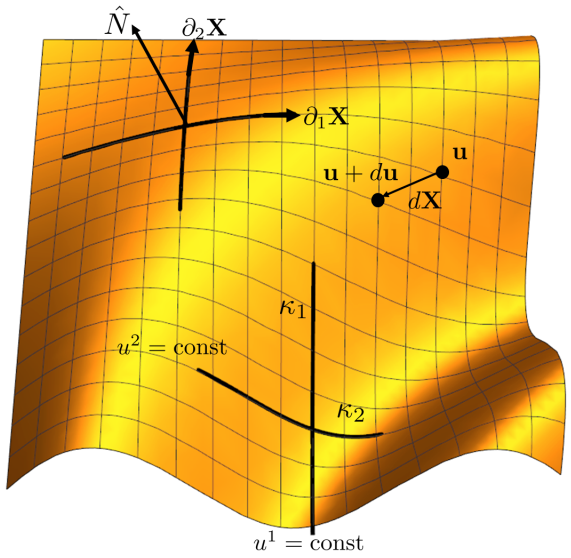

Figure 3.1. u^1 and u^2 are the (arbitrary) coordinates chosen to parametrize the surface. Curves with constant coordinate values are shown. The vector $d\mathbf{X}$ is the displacement vector between the points parametrized by $\mathbf{u}$ and $\mathbf{u}+d\mathbf{u}$. The displacement vector satisfies $|d\mathbf{X}|^2 = d\ell^2$, which leads to the definition in Eq. (3.1)

(V) studies the stability of elongating cylindrical shapes. After showing that purely geometric coupling alone is generically linearly unstable, we add the effect of coupling growth to stress and show that stability requires a combination of coupling to both curvature and stress. Finally, we conclude in Sec. (VI).

3.2 Differential Geometry of Surfaces

To establish notation, we give a brief overview of the differential geometry of surfaces in three dimensions [42, 43]. Throughout this chapter we assume Einstein's summation convention, where repeated indices are summed unless otherwise stated. A surface embedded in 3D Euclidean space can be represented as a vector function of two variables, $\mathbf{X}(u^1, u^2) \equiv \mathbf{X}(\mathbf{u})$, as in Fig. (3.1). Information about the shape of the surface is encoded in the length and curvature of curves $\mathbf{u}(\ell)$ on the surface, parametrized by their arc length ℓ. The length of any curve can be determined from

the metric tensor through the relation

$$d\ell^2 = (\partial_i \mathbf{X} \cdot \partial_j \mathbf{X})\, du^i du^j \equiv\ g_{ij}\, du^i du^j \tag{3.1}$$

where ∂_i is the partial derivative with respect to the coordinate u^i. Likewise the curvature tensor determines the curvature of curves in the direction normal to the surface through the relation (Fig. 3.1)

$$\kappa_N \equiv (\partial_i \partial_j \mathbf{X} \cdot \hat{N})\, \frac{du^i}{d\ell}\frac{du^j}{d\ell} \equiv b_{ij}\, \frac{du^i}{d\ell}\frac{du^j}{d\ell}. \tag{3.2}$$

Derivatives of tangent vectors can be expressed through the covariant derivative, formally defined on vectors as $D_i v_j = \partial_i v_j - \Gamma^k_{ij} v_k$ and $D_i v^j = \partial_i v^j + \Gamma^j_{ik} v^k$, where the Levi-Civita connection, Γ^j_{ik} is given by

$$\Gamma^j_{ik} = \frac{1}{2} g^{jl} \left(\partial_i g_{kl} + \partial_k g_{il} - \partial_l g_{ik}\right). \tag{3.3}$$

On the other hand, the covariant derivative of a scalar function, $\phi(\mathbf{u})$, is the same as the coordinate derivative, so $D_i \phi = \partial_i \phi$. The failure of the covariant derivatives to commute measures the Ricci curvature of a surface, R. In particular,

$$[D_i, D_j] v^k = \frac{R}{2} \left(g_{jl}\, \delta^k_i - g_{il}\, \delta^k_j\right) v^l. \tag{3.4}$$

On the other hand, $D_i D_j \phi = D_j D_i \phi$.

We distinguish between the reference metric $\bar{g}_{ij}$ and the actual metric g_{ij}. The reference metric, $\bar{g}_{ij}$, encodes the local equilibirum lengths along any sufficiently small patch of the surface. Deviations of the actual metric from the target metric is encoded in the strain tensor $\epsilon_{ij} \equiv g_{ij} - \bar{g}_{ij}$. Growth can be represented as changes in the rest lengths on the surface. In other words, $\bar{g}_{ij}(t)$ will be time dependent. Since bending

energy is negligible, the time dependence of the target curvature tensor $\bar{b}_{ij}$ will be of secondary importance.

Finally, we give the definition of the Gaussian, K, and mean, H, curvatures:

$$2H \equiv g^{ij}\, b_{ij} \quad \text{and} \quad K \equiv \frac{\det(b_{ij})}{\det(g_{ij})}, \tag{3.5}$$

where g^{ij} is the matrix inverse of the metric g_{ij}, implying $g^{ij}g_{jk} = \delta^i{}_k$. Finally, note that by considering the matrix $b^i_j \equiv g^{ik}b_{kj}$, we can define two principal curvatures, κ_1 and κ_2, as the eigenvalues of b^i_j along with their associated principal directions. These principal curvatures represent maximal and minimal normal curvatures of curves passing through a point and, thus, they are coordinate invariants. They are related to the Gaussian and mean curvatures through the relations $K = \kappa_1\kappa_2$ and $2H = \kappa_1 + \kappa_2$.

It is well known that, if g_{ij} and b_{ij} satisfy compatibility conditions expressed through the Gauss-Codazzi-Mainardi equations, then they are sufficient to uniquely determined the surface up to rigid transformations. These compatibility relations specify that

$$\begin{aligned} R &= 2K \\ D_i b_{jk} &= D_j b_{ik}. \end{aligned} \tag{3.6}$$

In that sense, we have a complete characterization of any surface in three dimensions from g_{ij} and b_{ij} alone.

3.3 Accounting For Dynamics

We start from the beginning (1666 AD), with Newton's laws in a viscous medium

$$\sigma_M\, \partial_t^2 \mathbf{X}(\mathbf{u},t) = -\gamma_D\, \partial_t \mathbf{X} - \frac{\delta_c E[\mathbf{X}]}{\delta_c \mathbf{X}} + \mathbf{f}(\mathbf{u},t), \tag{3.7}$$

where σ_M is the surface mass density and γ_D is a drag coefficient, $E[\mathbf{X}]$ is the elastic energy, $\mathbf{f}$ is an externally applied force, and the functional derivative is defined as $\delta_c/\delta_c\mathbf{X} = \delta/(\sqrt{g}\,\delta\mathbf{X})$. With this definition $-\delta_c E[\mathbf{X}]/\delta_c\mathbf{X}$ gives the elastic force per unit area.

It is well known that the elastic energy of thin shells is composed of a stretching part, which is proportional to the thickness, τ, and a bending part, which is proportional to τ^3 [57, 58, 59]. Unlike stretching, bending deformations do not stretch the mid-surface of the shell. A quick experiment with paper will convince you that it costs much less energy to bend a thin sheet than it does to stretch it. Specifically, we take the elastic energy to be

$$E_{el} = \int d^2u\sqrt{g}\left[\eta_S\, A^{ijk\ell}\,\epsilon_{ij}\epsilon_{k\ell} + \eta_B\,(H - H_0)^2\right]. \tag{3.8}$$

We have defined $\eta_S \sim \tau$ and $\eta_B \sim \tau^3$ to absorb numerical factors. We also introduced the elasticity tensor $A^{ijk\ell} \equiv \lambda\bar{g}^{ij}\bar{g}^{k\ell} + 2\mu\bar{g}^{ik}\bar{g}^{j\ell}$, where λ and 2μ are the Lamé constants, which can be expressed in terms of Young's modulus Y and Poisson's ratio ν as

$$\lambda \equiv \frac{Y\,\nu}{(1+\nu)(1-2\nu)}, \quad \text{and} \quad 2\mu \equiv \frac{Y}{1+\nu}. \tag{3.9}$$

The bending energy in Eq. (3.8) is slightly different from the standard choice $A^{ijk\ell}(b_{ij} - \bar{b}_{ij})(b_{k\ell} - \bar{b}_{k\ell})$. Since – for extremely thin shells – the bending energy is subdominant, we do not expect this choice to change the overall analysis. Furthermore, when the reference curvature is isotropic, it can be written as $\bar{b}_{ij} = \bar{\kappa}\,\bar{g}_{ij}$, with $\bar{\kappa}$ being the two principal curvatures. With this choice the two energies become essentially equivalent as $\tau \to 0$.

In these expressions, the growth is implicit: $\bar{g}(t)$ is assumed to be a slowly-varying function of time. Due to the separation of growth and elastic time scales, we assume

the elastic energy is minimized at each instant, with a quasi-static background metric. In the next section, we will account for the coupling between the reference metric and the shape of the shell.

3.4 Accounting For Growth

In order to have a complete description of a growth process we need to specify how the background metric $\bar{g}_{ij}(t)$ changes with time. A generic class of growth laws can be described by giving the rate of change of the metric as a function of the shape, $\partial_t \bar{g}_{ij}(t) = F[\mathbf{X}]$. We will assume that $F[\mathbf{X}]$ is a local function of the shape, expressed in terms of the geometrical invariants already introduced. This is consistent with the notion that material insertion is determined from local information only.

There is of course, an infinite variety of possible growth laws consistent with this form; in this section we derive the most general growth law consistent with symmetries. Stated simply, locality is the assumption that the instantaneous change in the metric at a certain position depends only on quantities defined on the surface at that point. Coordinate invariance implies that the instantaneous change in the metric should be a rank-2 tensor on the surface. We assume that this tensor only depends on the local shape (principle of shape dependence) and an applied stress (strain) tensor, which severely restricts the form of the growth law. The constraints on the form of the growth law are coordinate invariance, locality and time homogeneity.

We start by describing the geometry dependent terms in the growth law, then we turn to stress-coupled growth. We end this section by trying to provide an intuitive understanding of the growth law contributions.

3.4.1 Geometric Coupling

Deriving the geometric growth terms, in the vicinity of some arbitrary point with coordinates $\mathbf{u}$, is most conveniently done by transforming into a coordinate system

where the metric at t = 0 is given by the identity matrix $\tilde{g}_{ij} = \delta ij$. This requirement however still does not fix the coordinate system. if the principal curvatures satisfy $\kappa_1 \neq \kappa_2$, then the coordinate axes are fixed by requiring the curvature tensor to have the form

$$\tilde{b}_{ij}(\mathbf{u}) = \begin{pmatrix} \kappa_1(\mathbf{u}) & 0 \\ 0 & \kappa_2(\mathbf{u}) \end{pmatrix}. \tag{3.10}$$

By locality, we mean that the mechanism responsible for generating the growth only has access to local shape information. To leading order in the vicinity of a point, the shape of the surface is defined by the two principal curvatures, and their directions. The principal directions can be taken without loss of generality to be in the u^1 and u^2 directions.

In an infinitesimal time step dt the metric changes by an amount given by

$$\tilde{G}_{ij}(\kappa_1, \kappa_2) = \begin{pmatrix} f_1(\kappa_1, \kappa_2) & f_3(\kappa_1, \kappa_2) \\ f_3(\kappa_1, \kappa_2) & f_2(\kappa_1, \kappa_2) \end{pmatrix}, \tag{3.11}$$

so that the new metric is $\tilde{g}_{ij} = \delta_{ij} + dt\ \tilde{G}_{ij}$. As mentioned, in this coordinate system $\tilde{G}_{ij}$ can only be a function of κ_1 and κ_2. To anticipate the form of this growth law in a general coordinate system we rewrite it in the form

$$\tilde{G}_{ij} = F_1(\kappa_1, \kappa_2)\ \delta_{ij} + a_0\ F_2(\kappa_1, \kappa_2)\ \tilde{b}_{ij} + F_3(\kappa_1, \kappa_2)\sigma^x_{ij}, \tag{3.12}$$

where σ^x_{ij} is a Pauli matrix and a_0 is a length scale characterizing the size of the shell. When $\kappa_1 \neq \kappa_2$, the matrices δ_{ij}, $\tilde{b}_{ij}$ and σ^x_{ij} form a complete basis over the space of 2×2 symmetric matrices. In that case, it is possible to express a general choice of the functions (f_1, f_2, f_3) in terms of (F_1, F_2, F_3). However, in the case $\kappa_1 = \kappa_2$ the curvature tensor will also be proportional to the identity matrix. To avoid this

problem, we might have replaced $\tilde{b}_{ij}$ with σ^z_{ij} as a basis matrix. However, as we will show next, this is not ideal if the growth process depends purely on the local shape.

When $\kappa_1 = \kappa_2$, it is not possible to uniquely chose coordinate axes at that point because in that case, all directions are equivalent as far as local shape is concerned. Consequently, the growth process cannot favor any direction in this situation. Thus choosing $\tilde{b}_{ij}$ which is proportional to the identity matrix when $\kappa_1 = \kappa_2$ is the proper choice. In addition, since as $u^1 \to -u^1$, $F_3(\kappa_1, \kappa_2) \to -F_3(\kappa_1, \kappa_2)$, the term proportional σ^x_{ij} is seen to violate chiral symmetry. Therefore, in the rest of this paper we will also take $F_3(\kappa_1, \kappa_2) = 0$. Finally, we write the growth law in a general coordinate system as

$$\partial_t \bar{g}_{ij} = F_1(H, K)\, g_{ij} + a_0\, F_2(H, K)\, b_{ij}. \tag{3.13}$$

Note that we wrote κ_1 and κ_2 in terms of H and K.

We may simplify the growth law by assuming that there is a small length scale λ controlling growth and sensing curvature. In the case of *E. coli* this length scale is the nanometer scale of proteins as opposed to the $a_0 \sim \mu m$ scale of the bacteria. Compared to the length scale λ, the curvatures can be considered small, which motivates a curvature expansion of the growth law.

$$\begin{aligned} F_{(1,2)}(H, K) \approx \alpha_{(1,2)} + \beta_{(1,2)}\, \lambda\, (H - H_0) - \\ \gamma_{(1,2)} \lambda^2\, (K - K_0) + \delta_{(1,2)} \lambda^2\, (H - H_0)^2, \end{aligned} \tag{3.14}$$

where we neglected terms of order λ^3. Note that terms of the form $|\kappa_1 - \kappa_2| = 2\sqrt{H^2 - K}$ are possible, but we neglect them due to their non-analyticity. For example, if $\mathbf{X}_S$ describes a sphere, then the rate of growth of a nearby surface $\mathbf{X}_S + \epsilon\, \delta\mathbf{X}$ will scale as $\partial_t g \sim O(\sqrt{\epsilon})$.

With that in mind, Eq. (3.14) represents the most general geometrically-coupled

growth law consistent with the assumed symmetries. Symmetry guarantees that spherical and cylindrical shapes will be fixed points of the evolution as we will show in Sec. 3.5. However, instabilities may lead to spontaneous symmetry breaking and non-symmetric fixed points.

Next we will consider general growth laws in the presence of externally applied tensors, such as the strain (stress) tensor.

3.4.2 Incorporating Stress Coupling

In this section, we seek growth laws that incorporate the role of the strain tensor, defined as $\epsilon_{ij} \equiv g_{ij} - \bar{g}_{ij}$.

We can write all the possible scalars and tensors that are consistent with our criteria. Raising and lowering are done only with g_{ij} and $\epsilon \equiv g^{ij}\epsilon_{ij}$. The different scalars that we can construct are

$$H,\ \epsilon,\ b^{ij}\epsilon_{ij},\ b_{ij}\,b^{ij},\ b^i_k\,b^{ij}\epsilon_{jk}, \bar{\nabla}^i\bar{\nabla}^j\epsilon_{ij},\ \cdots \tag{3.15}$$

The tensors are

$$\epsilon_{ij},\ g_{ij},\ b_{ij},\ \epsilon^k_i\,b_{kj},\ b^k_i\,b_{kj},\ \bar{\nabla}_i\bar{\nabla}_j\epsilon,\ \bar{\nabla}^k\bar{\nabla}_k\epsilon_{ij}\ \cdots \tag{3.16}$$

where ∇ and $\bar{\nabla}$ are the covariant derivatives associated with the metrics g_{ij} and $\bar{g}_{ij}$. Terms containing the covariant derivatives will be dropped since they are of order $O(\epsilon\,\lambda^2)$.

We can now construct the most general growth law neglecting terms of order $O(\lambda^3), O(\epsilon^2)$ and $O(\lambda^2\,\epsilon)$. Concretely, we have

$$\begin{aligned}\partial_t\bar{g}_{ij} = \alpha_1\,g_{ij} + \alpha_2\,b_{ij} + \beta_1\,H\,g_{ij} + \beta_2\,H\,b_{ij}\\ -\gamma_1\,K\,g_{ij} - \gamma_2\,K\,b_{ij} + \sigma_1\,\epsilon_{ij} + \sigma_2\,\epsilon\,g_{ij} + \sigma_3\,H\epsilon_{ij} +\\ \sigma_4\,H\,\epsilon\,g_{ij} + \sigma_5\,\epsilon\,b_{ij} + \sigma_6\,b^{k\ell}\epsilon_{k\ell}\,g_{ij} + \sigma_7\,\epsilon^k_i\,b_{kj}.\end{aligned} \tag{3.17}$$

Next, we will try to make sense of the various terms in this growth law.

3.5 Linear Stability of Elongating Cylinders

We now analyze the linear stability of elongating cylindrical shells under the growth law in Eq. (3.17). However, this analysis could be applied more generally, for example, to spherical and leaf-like shells. As mention earlier, spherical, planar, or cylindrical symmetries will tend be preserved under time evolution. Therefore surfaces with these symmetries form a kind of generalized fixed point. We say generalized because they may still be evolving, as in the case of the elongating cylinder. However, instabilities may cause spontaneous symmetry breaking to non-symmetrical shapes. using linear stability analysis we can determine under what parameter values a given symmetry is linearly stable.

We will start our analysis by considering purely geometric coupling, later we will consider the effect of adding the stress coupling terms.

3.5.1 Purely Geometric Coupling

As mentioned in Sec. 3.4.1, we will ignore terms which have dimensions of Length^{-1}, since these terms will be multiplied by a small length scale λ. The growth law in the purely geometric case is

$$\begin{aligned}\partial_t \bar{g}_{ij} = \alpha_1\, g_{ij} + \alpha_2\, a_0\, b_{ij} + \beta_1\, a_0\, (H - H_0)\, g_{ij} + \\ a_0^2\, \beta_2\, (H - H_0)\, b_{ij} - a_0^2\, \gamma_1\, (K - K_0)\, g_{ij}.\end{aligned} \tag{3.18}$$

Here H_0 and K_0 represent some time-independent reference curvatures, their definition can be absorbed into $\alpha_{(1,2)}$. We will take them to be the mean and Gaussian curvatures of the fixed point solution. For a sphere with initial radius a_0, we will have $H_0^2 = K_0 = 1/a_0^2$. Naturally for a flat fixed point we would chose $K_0 = H_0 = 0$. Finally, for an elongating cylinder with radius a_0 we will chose $K_0 = 0$ and $H_0 = -1/2a_0$.

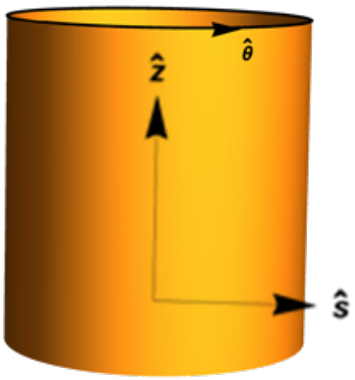

Figure 3.2. A coordinate system describing an elongating cylinder. The coordinate z, along the $\hat{z}$ direction, is normalized such that $z \in (0, 1)$.

We've neglected a term proportional to $(H - H_0)^2$ since it will not be important for linear stability.

We start by seeking elongating cylindrical solutions of the form

$$\begin{aligned} \mathbf{X}_{Cyl} &= a\ \hat{s}(\theta) + z\ L(t)\ \hat{z} \\ \bar{g}_{ij} &= \begin{pmatrix} L_0^2(t) & 0 \\ 0 & a_0^2 \end{pmatrix}, \end{aligned} \tag{3.19}$$

where $\hat{s}$, $\hat{z}$ and $\hat{\theta}$ are the cylindrical basis vectors (see Fig. 3.2). Here $z \in [0, 1]$ and $L_0(t)$ is the time dependent length of the shell. The definition of z is convenient because it allows us to consider a boundary value problem on the domain $z \in [0, 1]$ instead of a time dependent domain $[0, L_0(t)]$. Furthermore, note that z and θ are thought of as material coordinates. In other words, if a given point on the shell was properly tagged and followed, its trajectory would be given by $\mathbf{X}(z, \theta, t)$, where (z, θ) are the coordinates on the initial cylinder at time $t = 0$.

In order to study the stability of the solution in Eq. (3.19), we need to first verify that it is a solution of the growth and elastic equilibrium equations in the absence of stress coupling. We assume $\bar{H} = H_0$, which implies that bending and stretching

energies prefer the same radius a_0. By plugging Eq. (3.19) into the elastic energy and minimizing with respect to a and L we find, as expected, $a = a_0$ and $L = L_0$. Of course, if $\bar{H} \neq H_0$ or we had nonzero pressure $p \neq 0$, then there will be small corrections to this answer. To find the time dependence of the length, we plug the ansatz Eq. (3.19) into the geometric growth law Eq. (3.18). Concretely, we get the conditions

$$\alpha_2 = \alpha_1, \quad \alpha_1 = 2\,R, \;\; \text{and} \;\; L_0(t) = \ell_0\, e^{R\,t}. \tag{3.20}$$

The first condition results from the requirement of fixed radius. As explained in appendix (C), a fixed radius emerges due to a balancing between isotropic expansion and inward volume contracting growth terms. A more physical way to say this, is that the α_2 term, which is proportional to b_{ij}, represent a slowing down of material insertion along any curved direction. Unlike the cylindrical case, a sphere has two nonzero curved directions, which implies that this balancing would lead to a halting of growth in all direction.

At this point we introduce a perturbation to the elongating cylinder, which has the form

$$\begin{gathered}
\mathbf{X}(z,\phi,t) = a\,[1+\rho(z,\phi,t)]\;\hat{s} + \\
L(t)\,[z+h(z,\phi,t)]\,\hat{z} + a\,\psi(z,\phi,t)\hat{\phi}, \\
\bar{g}_{ij} = \begin{pmatrix} L_0(t)^2 + G_{zz}(z,\phi,t) & G_{z\phi}(z,\phi,t) \\ G_{z\phi}(z,\phi,t) & a^2 + G_{\phi\phi}(z,\phi,t) \end{pmatrix}.
\end{gathered} \tag{3.21}$$

Plugging this into the growth equations (3.18) and assuming the conditions (3.20) gives us a set of three coupled partial differential equations, which are second order in spacial coordinates and first order in time. However, since we have six unknown function in Eq. (3.21), we need to use the three elastic equilibrium equations. This

is more easily done in Fourier space, which is possible since the equations are linear and the reference solution has cylindrical symmetry. Specifically, we have

$$\rho(z,\phi,t) = \sum_m \int \frac{dq}{4\pi^2}\, \rho_{mq}(t)\, e^{im\phi}\, e^{iqz} \tag{3.22}$$

And similarly for other functions. periodic boundary conditions in the ϕ direction are implied in this expansion. A more realistic basis in the z direction would be $\sin(n\pi z)$, with $n = 1, 2, \cdots$. However, the expression for the growth rate of perturbations will not depend on this choice as long as we keep in mind that $q_{min} \sim 1/\pi$.

We will solve the equations in two steps. First, we solve the elastic equilibrium equations for the components of $\bar{g}_{ij}$, then we use the growth equations to find the growth rate of radial perturbations $R_\rho(m,q) \equiv \dot{\rho}_{mq}/\rho_{mq}$. The elongating cylinder will be stable if $R_\rho < 0$ for all excitable modes. Since the resulting algebra is too long to show here, we will only show the results in the $\eta_B \to 0$ limit. However the finite thickness results will be plotted and discussed.

We first need to find the elastic equilibrium equations. To leading order, the elastic energy can be written as

$$\begin{aligned} E_{el} = \sum_{\mathbf{m}} \int \frac{dz\; d\phi\; d^2\mathbf{q}}{4\pi^2} e^{i(m_1-m_2)\phi}\; e^{i(q_1-q_2)z}\; E_{\mathbf{mq}}[\rho_{\mathbf{mq}}, h_{\mathbf{mq}}, \psi_{\mathbf{mq}}] = \\ \sum_m \int dq\; E_{mq}[\rho_{mq}, h_{mq}, \psi_{mq}], \end{aligned} \tag{3.23}$$

where $\mathbf{m} = \{m_1, m_2\}$ and $\mathbf{q} = \{q_1, q_2\}$. We can find the equilibrium equations by taking the derivatives of the energy with respect to the independent variable. Specifically

$$\frac{\delta E_{mq}}{\rho_{mq}} = \frac{\delta E_{mq}}{h_{mq}} = \frac{\delta E_{mq}}{\psi_{mq}}. \tag{3.24}$$

In the limit $\tau, \eta_B \to 0$, the solution to Eq. (3.24) is given by

$$\begin{aligned}
\rho_{mq} &= \frac{m^2\, G_{zz} - 2\, m\, q\, G_{z\phi} + q^2\, G_{\phi\phi}}{2\, a_0\, q^2}, \\
h_{qm} &= -\frac{i\, G_{zz}}{2\, q\, L_0^2} \qquad \text{and} \\
\psi_{mq} &= i\frac{m\, G_{zz} - 2\, q\, G_{z\phi}}{2\, a_0^2\, q^2},
\end{aligned} \tag{3.25}$$

which is an isometry of the metric given in Eq. (3.21). Alternatively, we can invert Eq. (3.25) to eliminate the components of $\bar{g}_{ij}$ from the growth equations. After plugging the resulting answer in the growth law, we obtain three first order ODEs for the functions $\rho_{mq}(t)$, $h_{mq}(t)$ and $\psi_{mq}(t)$. For the case $\eta_B \to 0$, the growth equations become

$$\begin{aligned}
\frac{\dot{\rho}_{mq}}{\rho_{mq}} &= -\frac{1}{4}\left(\Gamma_1 + q_P^2\, \Gamma_2 + m^2\, \Gamma_3 + \frac{m^2(m^2-1)\Gamma_4}{q_P^2}\right), \\
\dot{h}_{mq}(t) &= -\frac{im}{4}\left(\Gamma_5 + \frac{(m^2-1)\, \Gamma_4}{q_P^2}\right)\rho_{mq}(t) \qquad \text{and} \\
\dot{\psi}_{mq}(t) &= -\frac{im}{4}\left(\Gamma_5 + \frac{(m^2-1)\, \Gamma_4}{q_P^2}\right)\rho_{mq}(t),
\end{aligned} \tag{3.26}$$

were we introduced the physical wavenumber as $q_P \equiv a_0\ q/L_0(t)$. With this definition, the instantaneous wavelength of the deformation is $\lambda_P = a_0(2\pi/q_P)$. It is interesting to note that even though q is time independent, q_P is not. This is due to the stretching of the wavelengths during elongation. We have also introduced the (q_P, m) independent rates Γ_i, which are given by

$$\begin{aligned}
&\Gamma_1 = \beta_2 - \beta_1 - 4R, \;\; \Gamma_2 = 2\gamma_1 + \beta_1 - \beta_2, \\
&\Gamma_3 = 2\, \gamma_1 + 2\, \beta_1 - \beta_2, \Gamma_4 = \;\beta_1 \\
&\text{and} \;\; \Gamma_5 = 2\gamma_1 + \beta_1 - 4R.
\end{aligned} \tag{3.27}$$

Note that h_{mq} and ψ_{mq} satisfy the same equation and they both approach a constant value when $\rho_{mq} \to 0$. It turns out, this last fact is true for any coordinate invariant growth law. This is easy to see by considering Eq. (3.21) with $\rho, \psi, \dot{h} \to 0$, for which the surface becomes $\mathbf{X} = a_0\ \hat{s} + L(t)(z + h_0(z, \phi))$. Its not too hard to convince yourself that this surface is still cylindrical. In other words, this deformation is equivalent to a coordinate transformation. Since the growth law is coordinate independent, a deformation with arbitrary $h_0(z, \phi)$ is a fixed point solution, which, just as Eq. (3.19), describes an elongating cylinder. This explains why $\dot{h}_{mq} = 0$ when $\rho_{mq} = 0$. A similar argument can be given for ψ_{mq} in the linear regime.

Thus, a sufficient and necessary condition for linear stability is $\rho_{mq}(t \to 0) = 0$, or that $R_\rho \equiv \dot{\rho}_{mq}/\rho_{mq} < 0$ for all permissible wavenumbers q_P and m. However, there is a subtlety associated with this stability condition.

As mentioned above, q_P is time dependent and as the wavelength of a solution is stretched, its rate of growth will also change. In particular, it is conceivable that $R_\rho > 0$ for a given q_P, but the solution is still stable. This is because the solution only experiences this instability for a short period of time before the physical wavelength q_P changes to value where $R_\rho < 0$. Keep in mind however, that this only happens if $R_\rho > 0$ for a small range of q_P, at the onset of an instability. In addition, some long wavelength instabilities might not be realized until the shell length $L_0(t)$ reaches a certain value.

Keeping all of that in mind, we derive the necessary condition for stability of all modes as $t \to \infty$, which implies $R_\rho < 0$ for all q_P and m up to a high cutoff.

From Eq. (3.26) we find the rate of growth to be

$$R_\rho = -\frac{1}{4}\left(\Gamma_1 + q_P^2\ \Gamma_2 + m^2\ \Gamma_3 + \frac{m^2(m^2-1)\Gamma_4}{q_P^2}\right). \tag{3.28}$$

A more complicated expression also exists in the finite thickness regime which, interestingly, also depends on the combinations Γ_i. Apart from the growth law param-

eters, R_ρ depends only on the physical wavelengths in units of a_0. The wavenumber m can in principle be any integer, however there will be a high cutoff value corresponding to a small length scale. q_P on the other hand will have a lower bound as well, corresponding to the finite size $L_0(t)$. Interestingly this lower bound is time dependent, decreasing with time. To zeroth order, we will require stability for all m and all q_P without bounds.

We first find the stability region in parameter space for the zero thickness case. Then we will see how finite thickness changes the situation. It is obvious from Eq. (3.28) that we must have $\Gamma_1, \Gamma_2, \Gamma_3, \Gamma_4 > 0$. This leads to the conditions

$$\beta_1 > 0, \quad \beta_2 > 4R + \beta_1, \quad 2\gamma_1 > \beta_2 - \beta_1 \tag{3.29}$$

This defines three planes that bound the stability region in parameter space. Fig. (3.3) shows a cross section of this region along with modes of instability when $\sigma_1, \sigma_2, \eta_B > 0$, which will be discussed shortly. In fact, this is also the region of stability for the finite thickness and stress coupling cases.

Now we turn to the interesting question of what happens near the three boundary surfaces of the stability region. Consider approaching the boundary $\Gamma_1 = 0$, while $\Gamma_2, \Gamma_3, \Gamma_4 > 0$. It is easy in this case, to see that the rate is maximized when $m = 0$ and $q_P \to 0$. This is illustrated in Fig. (3.4). It can also be seen readily from Eq. (3.28) that crossing the boundary $\beta_1 = 0$ results in modes with high $m \sim m_{cutoff}$ and small $q_P \sim a_0\pi/L_0$ dominating the shape. Here m_{cutoff} is the mode number at which our long wavelength approximation fails. However, finite thickness regularizes this behavior. As can be seen from Fig. (3.5) the instability in the finite thickness case happens at $m = 2$ and $q_P \sim 0.2$.

We may also get an instability that favors modes of high $q_P \sim q_{cutoff}$ by setting $\Gamma_2 < 0$. Unfortunately in this case, the bending energy does not regularize the

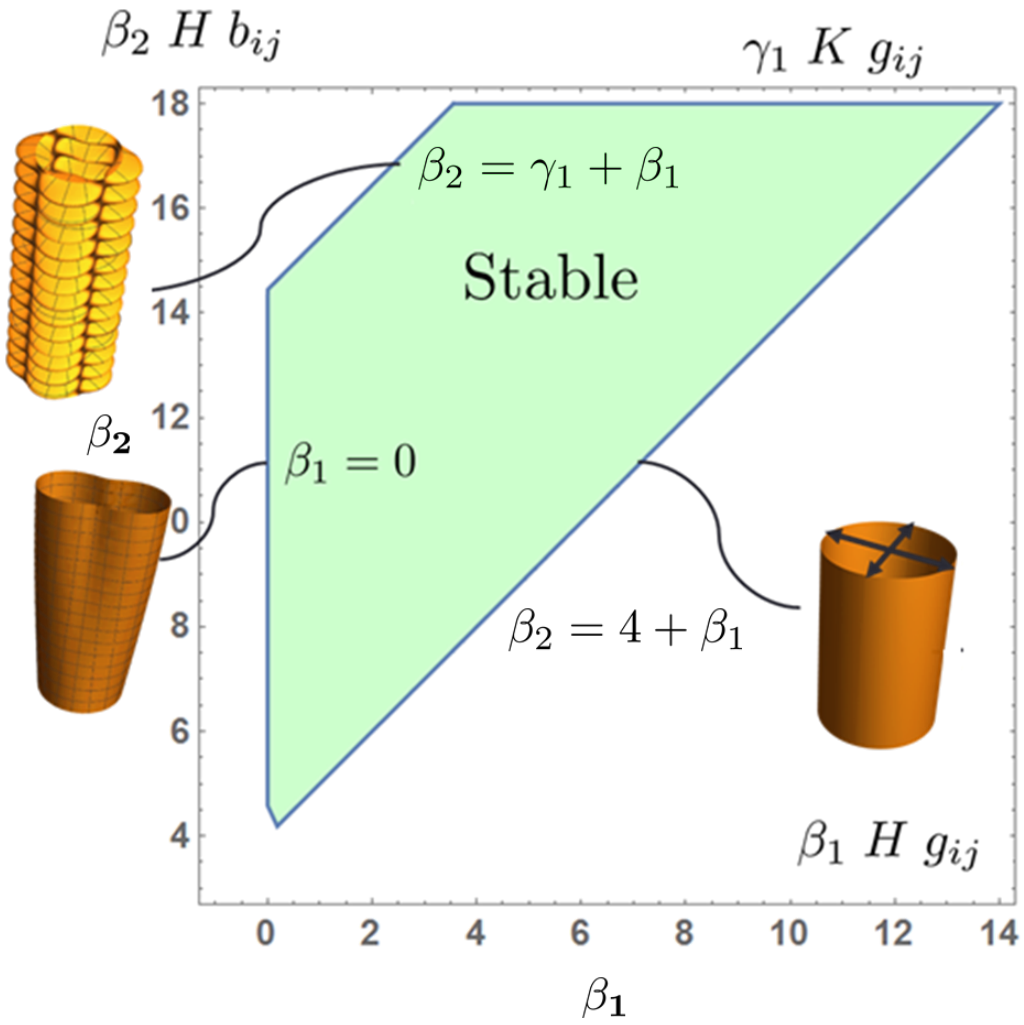

Figure 3.3. This figure shows the stability region in the (β_1, β_2) plane with $\gamma_1 = 9$ and stress coupling $\sigma_1 = \sigma_2 = 10$. Here and in all plots $R = 1$, $a_0 = 1$, $\nu = 1/3$, $\eta_B = 0.01^3$ and $\eta_S = 0.01$. We also show the nature of the instabilities when crossing the different boundaries. The nature of these instabilities depends on $\sigma_1, \sigma_2, \eta_B > 0$, however the region itself would look the same in the case $\sigma_1, \sigma_2, \eta_B = 0$.

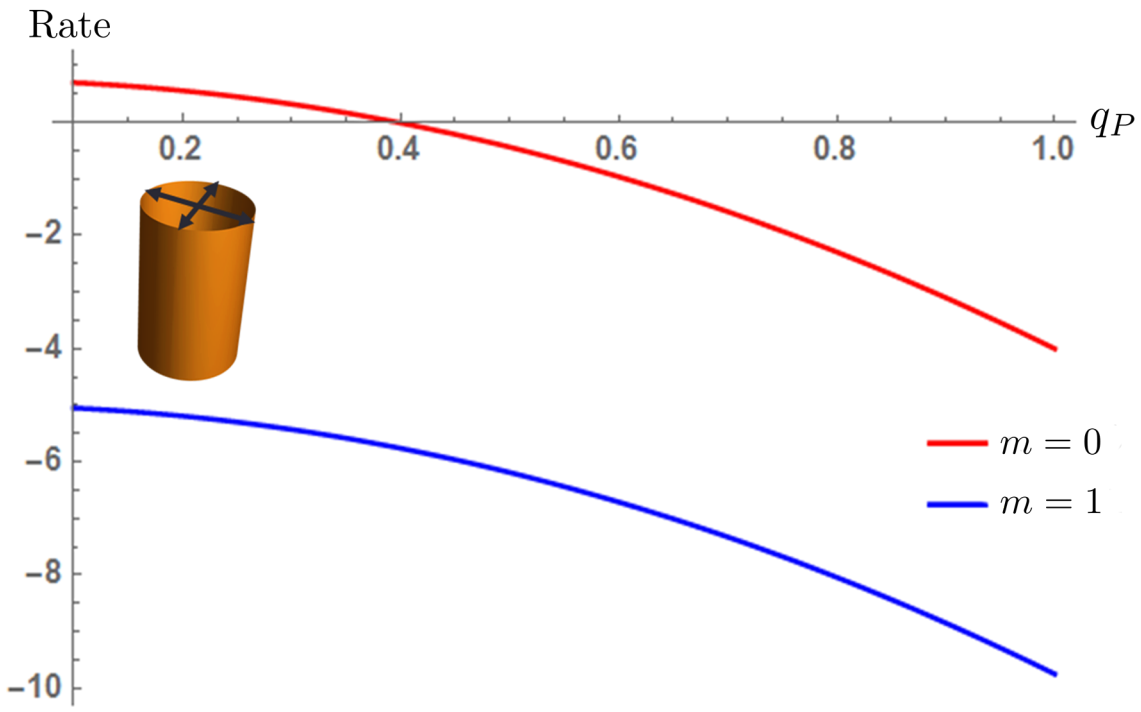

Figure 3.4. This figure shows the growth rate as function of q_P for different values of m when $\beta_2 < \beta_1 + 4R$. Note that the maximum rate happens at m $= 0$ and $q \sim 0$.

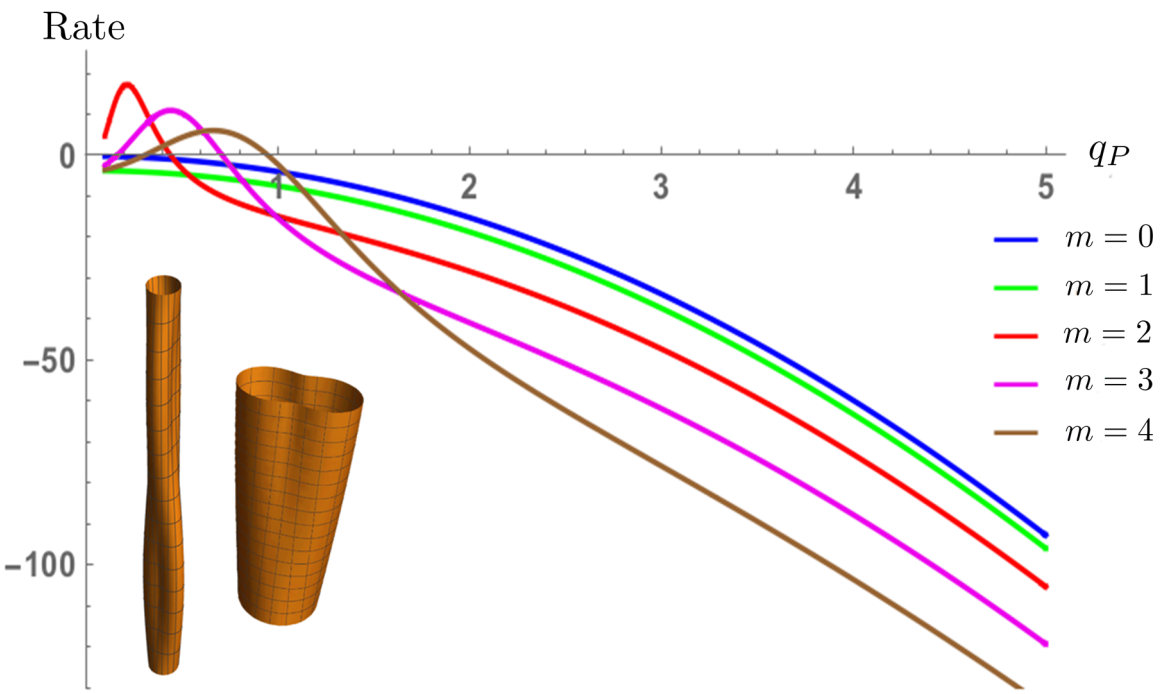

Figure 3.5. This figure shows the growth rate as function of q_P for different values of m when $\beta_1 < 0$. Note that the maximum rate happens at m = 2.

behavior at large q, and in fact, seems to make these modes more unstable. In particular, in the finite thickness case we have

$$\lim_{q_P \to \infty} R_{\rho B} = -\lim_{q_P \to 0} R_{\rho B} = -\lim_{m \to \infty} R_{\rho B} = 4\,R, \tag{3.30}$$

where the index B in $R_{\rho B}$ is added to emphasize that bending energy is considered. We see from Eq. (3.30) that the effect of bending energy is to make the high m modes always stable, while high q_P modes are unstable for all parameter values (see Fig. 3.6). This non-intuitive result is one of the main contributions of this paper.

The reason this is counter intuitive is because bending is expected to suppress modes of small wavelength rather than enhance them, which is true in the static setting. In a growing shell, to suppress the small wavelength fluctuations, their growth in the target metric must be suppressed. In the absence of bending, this suppression

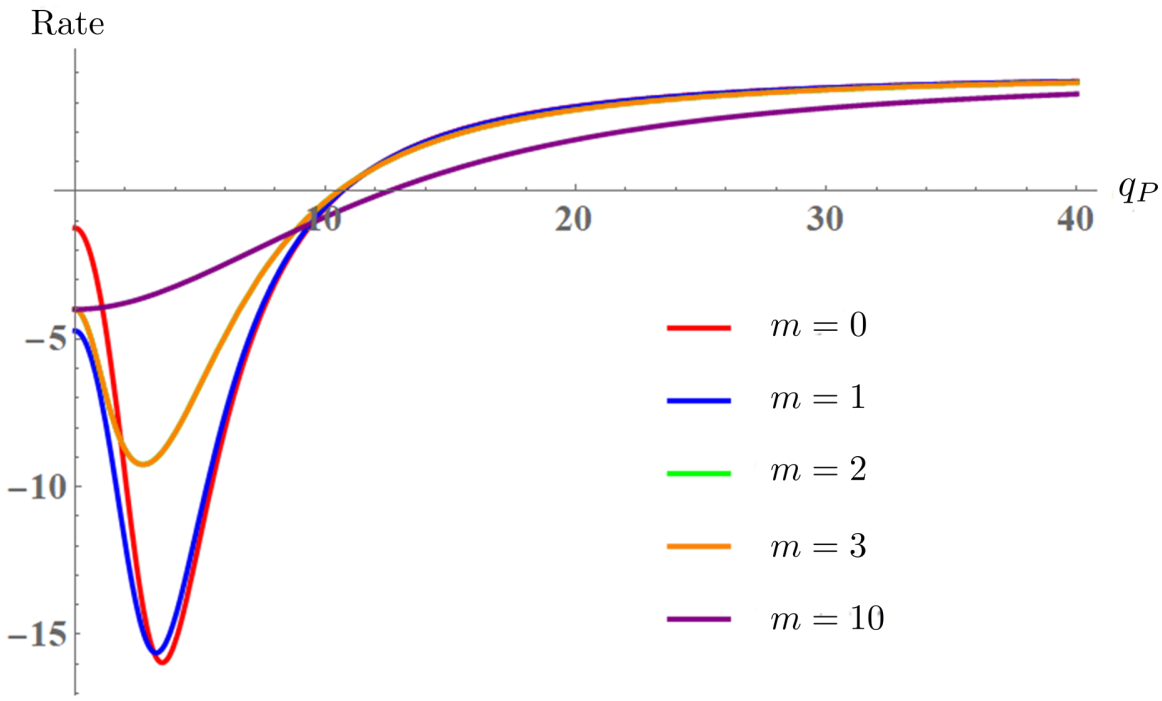

Figure 3.6. This figure shows that all modes are unstable in the absence of stress coupling for high values of $q_P > a_0/\tau$. Here we set $\eta_S^3 = \eta_B = 0.3^3$, $\beta_1 = 5$, $\beta_2 = 14$, $\gamma_1 = 9$, $\sigma_{1,2} = 0$ and $\nu = 1/3$. Fig. 3.8 shows how stress coupling modifies and stabilizes this behavior.

happens through the Γ_2 term in Eq. (3.28). As we show in appendix (E), bending suppresses this term indirectly by inhibiting high curvature modes. Amazingly, by suppressing high curvature modes, you allow them to grow further in the target metric.

Regardless of the source of these instabilities, a growing shell – such as E. *coli* – must find a way to avoid these instabilities. One possibility is that the small wavelength cutoff, λ, is on the order of the thickness of the shell. This is a reasonable possibility since the expansion of the energy in powers of thickness breaks down. For wavelengths that are close to the thickness, the rate behaves as

$$R_{\rho B}(q_P \to \frac{a_0}{\tau}) = -4\,\frac{\Gamma_2 - R\,(1-\nu^2)}{1-\nu^2}. \tag{3.31}$$

Therefore, in the absence of stress coupling we must require that $\Gamma_2 > R\,(1-\nu^2)$ and $q_P \lesssim \tau$ to achieve stability. The appearance of the material parameter ν (Poisson's ratio) in this expression is due to its effect on the response of the shape to the bending force, which in turn affects the growth rate.

Another, more robust way to stabilize small wavelength fluctuations is accomplished by coupling stress to the growth, which we turn to next.

3.5.2 Stress Coupling To The Rescue

As we have seen in appendix (C), the term $\sigma_1\ g_{ij}$ with $\sigma_1 > 0$ tends to make the target metric grow to comply with the applied force. So if the applied force is bending, then we may expect that adding stress coupling can lead to suppression of the modes $q_P \gtrsim \tau$. After ignoring terms of order $O(\lambda\,\epsilon)$ as described before, we step through the calculation in a similar manner to that described above. We eventually get

$$\lim_{q\to\infty} R_{\rho B} = 4\,R - \left(\sigma_1 + \frac{1-2\nu}{1-\nu}\sigma_2\right). \tag{3.32}$$

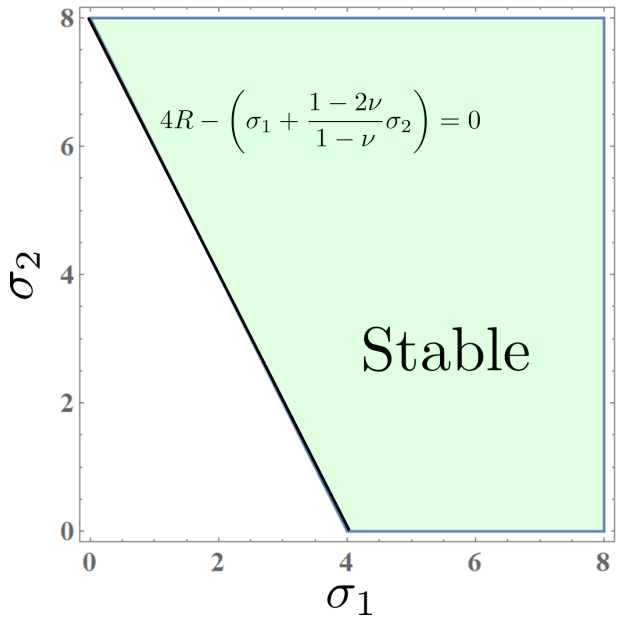

Figure 3.7. This figure shows the stability region in the (σ_1, σ_2) plane with $\gamma_1 = 9$, $\beta_1 = 6$ and $\beta_2 = 16$. Here and in all plots $R = 1$, $a_0 = 1$, $\nu = 1/3$, $\eta_B = 0.01^3$ and $\eta_S = 0.01$.

In other words if the stress coupling is strong enough, then small wavelength modes are always stable no matter what parameters you use. It can also be shown that the stability region in that case is the same as before (Figs 3.3 and 3.7). In addition, the $\beta_1 < 0$ and $\beta_2 < \beta + 4$ R instabilities still look the same (see Figs. 3.4 and 3.5). However, as Fig. (3.8) shows, when we cross the $\Gamma_2 = R\,(1-\nu^2)$ plane, the instability will not start at the highest q_P modes as before. In fact, it will happen typically for m = 2 and $q_P \sim O(10)$.

Thus, stress coupling enhances the stability against small wavelength deformations. And so, having both geometric and stress couplings can lead to stability of an elongating cylinder against all modes for a broad range of parameters.

Finally, we mention the possibility of stability with purely stress coupling. In other words, growth would stop in the absence of stress. In this case, elongation can be accomplished either due to pressure or incompatibility between the target metric

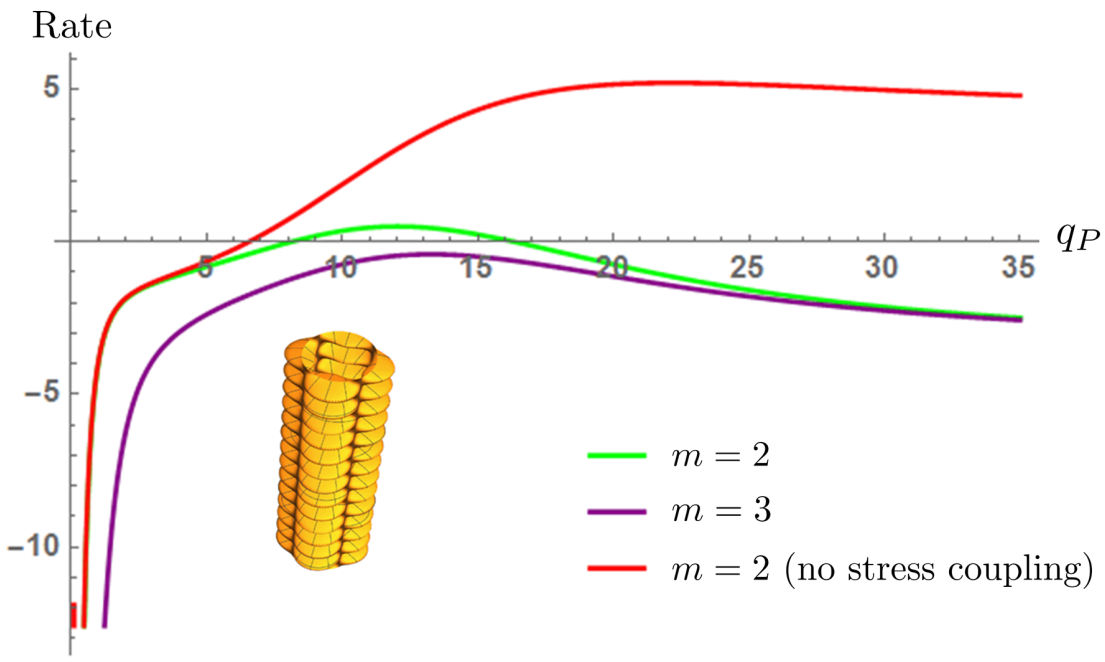

Figure 3.8. This figure shows the growth rate as function of q_P for different values of m when $\Gamma_2 < R\,(1-\nu^2)$ and $\sigma_1, \sigma_2 > 4R$. Note that the maximum rate happens at m = 2 and at a finite value of $q_P \sim O(10)$. For comparison, we have also included a plot of the rate in the absence of stress coupling.

and curvature tensors. However, we will not consider these possibilities in detail here since they will be part of future work. For now, we will consider the simpler question of what happens when we set the couplings $\beta_1 = \beta_2 = \gamma_1$. In this case, it can be shown that $R_\rho(m = 0) = R + O(\tau^2)$, which is unstable for all σ_1, σ_2. Roughly speaking, this indicates that geometric coupling might be important for the stability of long wavelength modes.

3.6 Conclusion

Growing elastic shells appear in a wide variety of contexts ranging from synthetic and natural shape changing materials that can be activated by spatially controlled swelling [50, 49] all the way to the growth of biomaterial sheets and planar tissues by the addition of material and proliferation of cells respectively [9, 47, 52]. In this paper, we have addressed for the first time, the dynamics of such growing sheets and the consequences for their stability. We have assumed that a growing shell, where material is getting added and removed, can be described with a slowly changing target metric, because, as a shell's structure rearranges, the natural distances between points in the shell change. Within this setup there are infinitely many ways that the metric can change with time. It could change in a prescribed shape-independent way, as done in experiments like [50, 49], it can be coupled to an externally applied field like a stress tensor or internal structure [55] or it can be dependent purely on shape as in Eq. (3.13).

Regulation of such growth to yield a desired structure typically requires a control mechanism. Such control mechanisms could couple the processes driving the growth to global properties of the shape, or to local properties of the shape, allowing the material to act locally and think globally. Therefore, in this paper we explored the coupling of the change in the metric to local properties of the sheet - the local shape, and a stress tensor. Symmetry and locality arguments help reduce the space of pos-

sible metric changes down to the form given in Eq. (3.17).

After constructing this general growth law, as a first step, we analyzed the linear stability of an elongating cylinder under purely geometric coupling (Sec. 3.5.1). Surprisingly, we found that for any choice of model parameters, modes with $q_P \sim 1/\tau$ cannot be stabilized (see Figs. 3.6,3.7). This unexpected result means that a growth law that is only shape-dependent cannot lead to an elongating cylinder that is linearly stable to small wavelength fluctuations.

Since biological systems appear to be able to solve this problem, we consider two possibilities. First, there might be a cutoff after which the assumptions under which our growth law will not be valid. One could imagine, for example that nonlinearities might result in the suppression of instabilities. However, even in such cases, one might expect to see the vestiges of the onset of the instability. This raises the intriguing possibility that such arrested instabilities could be used to create small scale patterns. To more robustly stabilize the growth, we consider a second mechanism, stress coupling , discussed in Sec. (3.5.2). In particular when the effects of stress coupling are included we find that these small wavelength modes become universally stable, as shown in Figs. (3.8,3.7). This is because the stress coupling terms tend to make the target metric grow in a viscoelastic-like way to conform with the applied forces as discussed in Appendix C. In this situation, the applied forces are the bending forces (in E. *coli*, turgor pressure contributes as well), and since small wavelength modes contribute a lot of bending energy they will be suppressed. Note that both the applied force and the stress coupling contribute to this result.

This work grew from interest in the stability of rod-like *E. coli*. We have shown how shape regulation can result from a combination of geometric and stress couplings. Interestingly, it was shown in [56] that coupling to areal strain alone can result in straightening of a bent rod. However, under this growth law a shell might still be unstable with respect to different modes of deformation. Experiments involving con-

trolled perturbations of the growth laws can yield a significant amount of information on the exact nature of the couplings. To this end, we are currently working on fitting the parameters of the model to experiments where bacteria are subjected to bending forces and oscillatory osmotic shocks resulting in perturbations in localizaation and dynamics of growth [55, 65]. One could also imagine directly probing the instabilties by growing *E. coli* in confining geometries with shapes of a specific wavelength in the z and ϕ directions. The exact form of R_ρ could then be compared to the results of the experiment.

Finally, it is also conceivable that a certain shape cannot be stabilized at all, just as we've seen that, with purely geometric coupling, an elongating cylindrical shell would always be unstable to small wavelength fluctuations. While flat, cylindrical and spherical shapes are fixed points of the growth law due to symmetry, an interesting project would be a characterization of all the possible stable shapes within this framework and relating them to the kinds of patterns observed in nature.

CHAPTER 4

OSMOTIC SHOCK

This chapter is concerned with applying the framework developed in chapter (3) to real experiments. While the formalism is meant to be applicable to generic growth problems, it is essential that we ground it in real world applications. Since cylindrically symmetric growth is easier calculate with, we will look for situations in which it is applicable. Osmotic shock experiments, that are done on E. *coli*, are a good target for our analysis. During an osmotic shock, a cell experiences a pressure drop or gain due to a sudden change in the concentration of some chemical, such as sorbitol [65].

There are difficulties in comparing osmotic shock experiments with results from our framework. First, since the chemical environment of the cell changes, it is not clear whether we are getting information about the growth pattern in the unperturbed cell, or about its stress response. Furthermore, the response of the cell to such a change will be complicated, comprising more than the change in growth pattern. For instance, the permeability of the cell membrane might be changing, giving rise to nontrivial time dependence of pressure. Another possible response we have to consider, is the cell wall becoming softer with time as a response to the osmotic shock.

Despite these disadvantages, it is still useful to study our model in the relatively solvable cylindrical growth scenario. Furthermore, analyzing the osmotic shock experiments in the context of our model has led to indirect model independent insights into these experiments.

4.1 Introduction

Entrant bacteria – that go into the intestines – such as E. *coli* likely face the challenge of maintaining stable growth under rapid changes in external pressure and osmolarity [66]. The mechanism by which this happens is not entirely understood. Furthermore, understanding the cell's response to osmotic shock will likely provide insight into how unperturbed E. *coli* maintain shape during growth and multiplication.

In [65], the authors subjected E. *coli* to hyperosmotic shocks (reduction of internal pressure) in order to gain insights into the mechanisms involved in cell shape regulation. An interesting feature of the response of E. *coli* to hyperosmotic shock, is stored or hidden growth.

Stored growth means that despite the slower growth rate during the shock, once the external conditions are restored, the bacterial cell wall expands back to the same shape that a completely untouched bacteria would have. In other words, the growth of the cell wall was being stored (or hidden) during the shock. This is illustrated in Fig. (4.1).

Cells can accommodate change in external conditions through mechano-sensitive channels, which help regulate the concentrations of different chemical, and consequently the osmotic pressure. Another possibility for regulation suggested in [65], is controlling the shape of building blocks being inserted into the growing cell wall. Later in this chapter, we will show that for any elastic materials, the stored growth phenomena requires precise pressure or Young's modulus time dependence.

4.2 The Theoretical Setup

We will first give a brief description of the experiment from a naive theorist perspective. During the experiment [65], the cell is subjected to different concentrations of sorbitol (400 - 2000)mM. Higher concentrations correspond to a bigger pressure

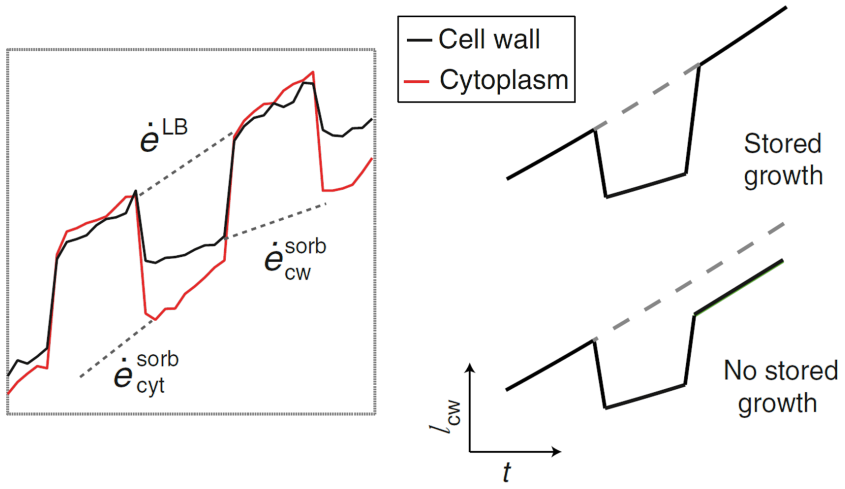

Figure 4.1. This plot demonstrates the hidden growth phenomena in E. *coli*. (Right) $\dot{e}^{LB}$ is the growth rate in the unperturbed scenario, whereas $\dot{e}^{sorb}_{cw}$ is the elongation rate of the cell wall after the shock. As the dashed lines indicate $\dot{e}^{sorb}_{cw} < \dot{e}^{LB}$. l_{cw} is the length of the cell wall. On the left, you can see the effects of stored (hidden) growth after restoration. This plot is adapted from [65]

drop. After the sudden pressure change, the response of the cell wall (radius and length) is measured with time.

We model the cell as a thin elastic pressurized cylindrical vessel, with potentially time-dependent rest length $\ell(t)$ and radius $a(t)$. The rest values $\ell(t)$ and $a(t)$, evolve according to the growth law we derived in the previous chapter (see Eq. 3.17). Cylindrical symmetry implies the ansatz

$$\mathbf{X}(t) = A(t)\,\hat{s} + L(t)\,z\,\hat{z}, \tag{4.1}$$

where $A(t)$ and $L(t)$ will be determined from the growth law and energy minimization. As before, $z \in (0, 1)$. Naturally, in the absence of external forces and pressure we will have $A(t) = a(t)$ and $L(t) = \ell(t)$.

Treating the cell as a thin pressure vessel we will have

$$\delta A \equiv \frac{A-a}{a} = \frac{Pa}{hY_\theta}\left(1-\frac{\nu}{2}\right) \quad \text{and}$$
$$\delta L \equiv \frac{L-\ell}{\ell} = \frac{Pa}{hY_z}\left(\frac{1}{2}-\nu\right). \tag{4.2}$$

Note that we've allowed for the possibility of having different Young's moduli in the θ and z directions. Under "normal" conditions, the cell will be under turgor pressure $P_{\text{Turgor}} = P_0$ and will have time independent Young's moduli. In that case, we define $\delta A_{\text{initial}} \equiv \epsilon_\theta$ and $\delta L_{\text{initial}} \equiv \epsilon_z$. Using experimental values for E. *ecoli* [61], we can estimate the actual values of these parameters as

$$\epsilon_z = \frac{P_0\, a_0}{2\, h\, Y_z^0} \approx 0.077 \quad \text{and} \quad \epsilon_\theta = \frac{P_0\, a_0}{h\, Y_\theta^0} \approx 0.072, \tag{4.3}$$

were the index zero represents the values unaffected by the osmotic shock. After the shock, pressure and Young's moduli will change with time. We can rewrite Eqs. (4.2) as

$$A(t) = a(t)\left(1+\epsilon_\theta\,\frac{p(t)\,a(t)}{y(t)\,a_0}\right) \quad \text{and}$$
$$L(t) = \ell(t)\left(1+\epsilon_z\,\frac{p(t)\,a(t)}{y(t)\,a_0}\right), \tag{4.4}$$

where $y(t) \equiv P(t)/P_0$ and similarly $y(t) \equiv Y_z(t)/Y_z^0 \equiv Y_\theta(t)/Y_\theta^0$. Note that for simplicity, we do not distinguish between y_θ and y_z. Interestingly, $p(t)$ and $y(t)$ will appear together as $a(t)\,p(t)/y(t) \equiv a_0/u(t)$.

Finally, we will adapt the growth law in Eq. (3.17) to the present situation with cylindrical symmetry and as before we will neglect terms of order $O(\lambda\epsilon)$ for simplicity. After a simple calculation we get

$$\frac{\partial_t[a(t)^2]}{A(t)^2} = \alpha_1 + \alpha_2\frac{a_0}{A} + \left(\beta_1 + \frac{\beta_2\, a_0^2}{A}\right)\left(\frac{1}{2a_0} - \frac{1}{2A}\right) + \delta_1\, a_0^2\left(\frac{1}{2a_0} - \frac{1}{2A}\right)^2 + (\sigma_1+\sigma_2)\frac{A^2-a^2}{A^2} + \sigma_2\frac{L^2-l^2}{L^2}$$
$$\frac{\partial_t[l(t)^2]}{L(t)^2} = \alpha_1 + \beta_1\left(\frac{1}{2a_0} - \frac{1}{2A}\right) + \delta_1\, a_0^2\left(\frac{1}{2a_0} - \frac{1}{2A}\right)^2 + (\sigma_1+\sigma_2)\frac{L^2-l^2}{L^2} + \sigma_2\frac{A^2-a^2}{A^2}, \tag{4.5}$$

were as before a_0 is the radius of E. *coli* under normal conditions. This completes the definition of the model.

4.3 Growth on a Normal Day

We start our analysis by establishing the growth behavior under normal conditions, or $u(t) = 1$. since we expect the behavior of the cell to be an exponential elongation with a fixed radius, the solution of Eq. (4.5) should be $a = a_0$ and $\ell(t) = \ell_0\, e^{R_0\, t}$. Plugging this ansatz into Eq. (4.5), we find that the parameters α_1 and α_2 must be

$$\begin{aligned}\alpha_1 &= 2R_0 - \epsilon_\theta\left(\frac{\beta_1}{2} + 2\sigma_2\right) - 2\epsilon_z\left(\sigma_1+\sigma_2+2R_0\right)\\ \alpha_2 &= 2R_0 + \epsilon_\theta\left(2R_0 - \frac{\beta_2}{2} + 2\sigma_1\right) - 2\epsilon_z\left(\sigma_1+2R_0\right).\end{aligned} \tag{4.6}$$

For simplicity, we will assume that this condition holds even during the osmotic shock.

Next, we consider stability of this elongating solution. We do this by deforming the ansatz slightly and giving it the form $\ell(t) = \ell_0 e^{R_0 t}\big[1+\delta\ell(t)\big]$ and $a(t) = a_0\big[1+\delta a(t)\big]$. Stability is established if $\delta a(t\to\infty) = 0$ and $\delta\ell(t\to\infty) = \text{const}$. This gives the condition $4R_0 + \beta_1 < \beta_2$. However, we do not demand that this condition be satisfied during a shock since the chemical environment of the growth process is different.

4.4 Stored Growth

We assume growth goes on normally until $t = 0$. Then suddenly, a hyperosmotic shock is applied, which we model as an instantaneous pressure reduction, i.e. p(t) =

$1 + \Theta(t)(p_f - 1)$. Here $\Theta(t)$ is the step function, which means that $p(t) = 1$ before the shock and $p(t) = p_f$ immediately afterwards.

Since ℓ and a are reference values and are pressure independent, the initial conditions resulting from this shock are, $\delta\ell(t = 0) = 0$ and $\delta a(t = 0) = 0$. On the other hand, $A(t)$ and $L(t)$ will experience a sudden elastic decrease at $t = 0$. It should be noted that $p(t)$ may not be time-independent after the shock due to mechano-sensing and response as mentioned earlier. We can however, absorb the time dependence of both $y(t)$ and $p(t)$ into the single function $u(t)$.

A very interesting behavior occurs in these experiments with cyclic shocking [65]. As illustrated in Fig. (4.1), the elongation rate slows down during the shock. However, when the pressure (or external condition) is restored, the length jumps to the value it would have if no shock was applied at all. This is strange since a lag in size would be expected due to the slowing down of growth. It's as if the growth had been stored or hidden during this process.

In order to appreciate the consequences of stored growth, assume that the pressure $p(t)$ does not change after the shock. Assume also, that after the external osmolarity is restored the pressure jumps to its original value $p(t) = 1$. With those assumptions in mind, we can now make a model independent statement: For any growth law, such that elongation slows down during the shock, but length is restored after the value of pressure is restored, the Young's modulus must be decreasing with time. This is not too hard to see, since the same change in pressure as the initial drop resulted in a bigger increase in length.

Starting from the experimental facts, we look at this argument in a little more detail. The experiments show – at least for shocks of small magnitude – that when the shock is applied, the growth slows down, which implies one of two things: either the growth of $\ell(t)$ and $a(t)$ slows down, or $\ell(t)$ and $a(t)$ are unchanged while $p(t)$ decreases. In either of these two cases, the actual lengths $L(t)$ and $A(t)$ would be

growing at a slower rate. In the second possibility, pressure would decrease further after the initial drop. Of course, a mix of these two possibilities can also be happening.

When the growth of $\ell(t)$ is in fact slowing down, we must find that $y(t)$ is decreasing with time. If Young's modulus $y(t)$ decreases in just the right way, then we will find that, as pressure is restored to $p = 1$, the length $L(t)$ will elongate to the desired unperturbed value. In the experimental paper [65], the suggested explanation of stored growth is that: While material insertion happened at the same rate, the inserted elements were buckled into smaller lengths. These buckled elements would over stretch when the pressure is restored. In the language of continuum mechanics, this is equivalent to Young's modulus becoming softer during the shock. Hence, we will focus on this possibility in the rest of this chapter.

Perfect recovery of length after a cyclic shock, will not happen with any time dependence of $y(t)$. In fact, $y(t)$ will be fixed by the condition $L(t, p = 1) = (1 + \epsilon_z)\, L_0(t)$. Using Eq. (4.4) we get

$$y(t) = \frac{\epsilon_z\, (1 + \delta a)(1 + \delta \ell)}{\epsilon_z - \delta \ell}. \tag{4.7}$$

The denominator seems problematic here, and possibly diverges at finite time (recall that $\delta\ell(t = 0) = 0$). This will not be a problem in our model since $\delta\ell < 0$ decreases with time under the shock. If instead we had an increasing $\delta\ell > 0$, the shell would be getting harder and approaching an infinite rigidity, which is closer to possibility number (2) above where $u(t)$ is increasing.

4.5 Fitting the Experimental Data

We are now in a position to solve for the evolution of the length and radius of a cell after a shock with magnitude $p(t = 0) = p_f$ is applied. Unfortunately, there are still

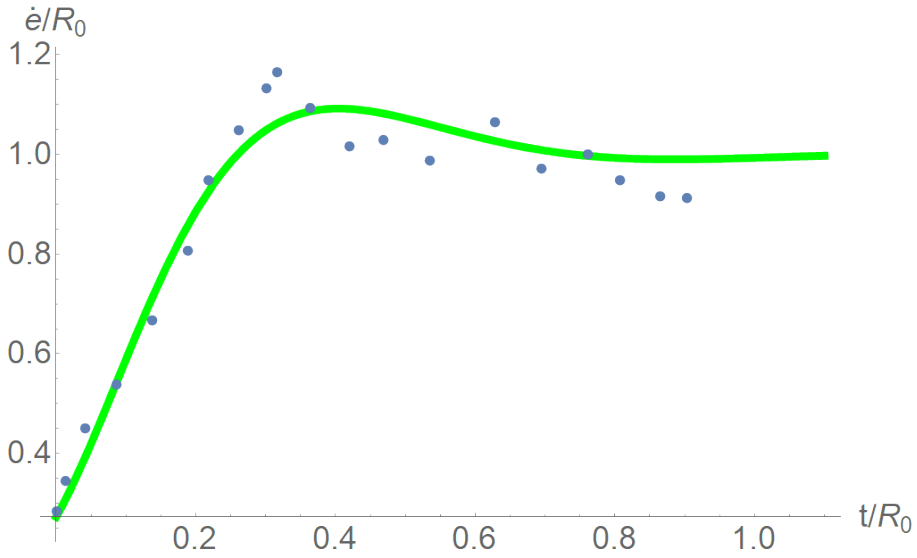

Figure 4.2. The elongation rate $\dot{e} \equiv \dot{L}(t)/L(t)$ is plotted vs. scaled time. Here, the fit is given by $p_f = 0.45, \sigma_1 = -17.67$, $\sigma_2 = 16.24, \beta_1 = 55.3, \beta_2 = 48.38$ and $\delta_1 = 10$. Points represent experimental data [65]

undetermined parameters in the model, and we will fit them to experimental data. Fig. (4.2) shows the result of such a fit and gives the value of the fit parameters.

Interestingly, the fit is sensitive to the value p_f – which sets the time scale of recovery – and only weakly determines the value of the other model parameters. Consequently, we can compare the fit value of pressure, $p_f = 0.45$, to the value of pressure expected from the initial elastic decrease in length and radius. We find from the experiments, that on average

$$\frac{L(0^-) - L(0^+)}{L(0^-)} = 0.045 \implies p_f = 0.41, \tag{4.8}$$

which is interestingly close to the value $p_f = 0.45$ from a completely independent fit.

An interesting feature of the experiments – which also appears in Fig. (4.2) – is the return of the rate to its unperturbed value at long time. This happens as a consequence of the stored growth condition in Eq. (4.7). In addition, Fig. (4.3) shows that even the radius evolves back to nearly its unperturbed value at long time.

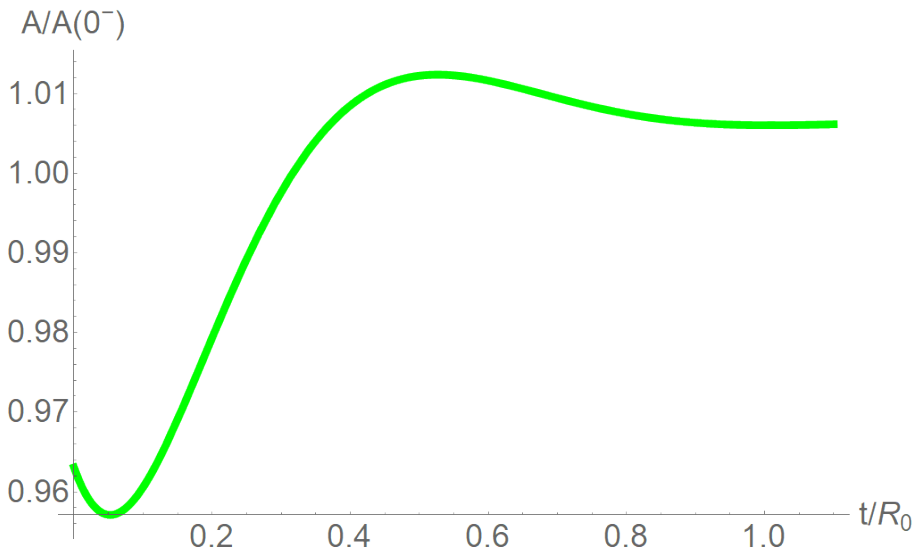

Figure 4.3. The evolution of the radius with time after the shock. As in Fig. (4.2), the fit is given by $p_f = 0.45, \sigma_1 = -17.67$, $\sigma_2 = 16.24, \beta_1 = 55.3, \beta_2 = 48.38$ and $\delta_1 = 10$. We find that $A(t \gg 1)/A(0^-) \approx 1.006$, compared to $A(0^+)/A(0^-) \approx 0.96$, showing evidence for radius regulation under different pressure values.

Which hints at an interesting radius regulation mechanism.

From the perspective of an entrant bacteria – which travels through environments with differing pressures – this makes a lot of sense. Not only is the initial radius restored if the original pressure is restored, even if staying permanently in the new pressure value, the initial value of the radius is approximately restored.

4.6 Conclusion

We have seen how the model developed in the previous chapter can be applied to real experiments. Since the model works on the effective level, and is not focused on the microscopic details – which can be very messy in the case of osmotic shock experiments – we can use it to gain clarity on the problem and to make some model independent statements.

We were able to think through the possibilities of explaining the phenomena of stored growth in a linear elastic material for any growth law. We then analyzed the possibility of a decreasing Young's modulus which is suggested from experiments. Furthermore, we are able to obtain a good fit of the experimental data using this assumption.

In the future, we will test this model on different shock magnitudes and compare the radius and length data simultaneously to experiments. An independent measurement of pressure and Young's modulus during the shock is essential for validating or rejecting the model.

We are also testing the model in different experimental scenarios. For instance, we are developing simulations to model the shape recovery of E. *coli* from different perturbations. In [67], authors have measured how a bacterial cell wall, after being forced to become spherical, recovers its original cylindrical evolution. Preliminary results show that we are able to reproduce this behavior within our growth model.

APPENDIX A

ISOMETRIES AND GEOMETRIC NONLINEARITIES

Here we will examine the nature of isometries from a general geometric perspective. This will provide us with guidance and a bird's eye view of what to expect for the isometry spectrum of a surface. The main two guiding principles will be Bonnet theorem [42] and the relationship between the normal and geodesic curvatures [38].

Let us start by considering the Gaussian curvature $K(g_{ij})$, which is a function of the metric. Gauss's theorema egregium states that

$$b_{12}^2 = b_{11}\kappa_N - K\rho^2, \tag{A.1}$$

using Gaussian normal coordinates [43], we have $d\ell^2 = (du^1)^2 + \rho^2(u^1, u^2)(du^2)^2$ and where $\kappa_N = b_{22}/\rho^2$ is the normal curvature along lines of constant u_1.

Under an isometry, the last term, $K\rho^2$ must remain constant. Eq. (A.1), together with

$$\begin{aligned} \partial_1 b_{12} &= \partial_2 b_{11} - b_{12}\frac{\partial_1 \rho}{\rho} \qquad \text{and} \\ \rho\partial_1\left(\rho\kappa_N\right) &= \partial_2 b_{12} + b_{11}\rho\partial_1\rho - b_{12}\frac{\partial_2\rho}{\rho}, \end{aligned} \tag{A.2}$$

form the Gauss-Codazzi-Mainardi (GCM) equations. Bonnet's theorem [42] states that if (A.1) and (A.2) are satisfied, a unique surface will be determined up to rotations and translations. Using this and the Cauchy Kowalevski (CK) theorem applied to the GCM equation, we can say something general about the local existence and

number of isometries without restricting ourselves to infinitesimal isometries.

Consider the vicinity of an arbitrary curve on the surface. Without significant loss of generality we assume this curve satisfies $u^1 = 0$. The CK theorem states that, as long as all the coefficients on the right-hand side of (A.2) are analytic, there will be a unique solution in the vicinity of the curve for an arbitrarily specified $b_{12}(u^1 = 0,\ u^2)$ and $\kappa_N(u^1 = 0,\ u^2) \neq 0$. In other words, the curve will have two isometric degrees of freedom as long as $\kappa_N \neq 0$ on the final deformed surface. However, κ_N may well be vanishing on the starting surface, as in the case of a torus. This is consistent with the inner solutions we found in section 2.3; we can specify $\delta_\pm$ and $\pm\sqrt{\gamma_\pm} \sim \kappa_N$ to determine the solution uniquely.

On the other hand, if at any point on the $u^1 = 0$ curve we have $\kappa_N = 0$ (on the final surface), the CK theorem fails and there is no guarantee of solutions. However, in this case, we can determine what happens by first expanding $b_{11} = b_{11}^{(0)}(u^2) + b_{11}^{(1)}(u^2)u^1$, $b_{12} = b_{12}^{(0)}(u^2) + b_{12}^{(1)}(u^2)u^1$, $\rho^2 K = K^{(0)}(u_2) + K^{(1)}(u^2)u^1$ and $\kappa_N = \kappa_N^{(1)}(u_2)u^1$, and collecting terms with common powers of $u^{(1)}$. We obtain

$$\begin{aligned} b_{11}^{(0)}\kappa_N^{(0)} - \left(b_{12}^{(0)}\right)^2 &= K^{(0)} \\ b_{11}^{(0)}\kappa_N^{(1)} + b_{11}^{(1)}\kappa_N^{(0)} - 2b_{12}^{(0)}b_{12}^{(1)} &= K^{(1)}. \end{aligned} \tag{A.3}$$

and so on. From Eqs. (A.2), we see that

$$\begin{aligned} b_{12}^{(1)} &= \partial_2 b_{11}^{(0)} + b_{12}^{(0)}\kappa_g^{(0)} \\ \kappa_N^{(1)} &= \kappa_g^{(0)}\kappa_N^{(0)} + \partial_2 b_{12}^{(0)} - \kappa_g^{(0)} b_{11}^{(0)}. \end{aligned} \tag{A.4}$$

where $\kappa_g = -\partial_1\rho$ is the geodesic curvature of the $u^1 = 0$ curve and $\rho(0, u^2) = 1$. Putting this together, we obtain a constraint in terms of the intrinsic geodesic curvature and Gaussian curvature in the vicinity of the curve,

$$K^{(1)} = b_{11}^{(1)}\kappa_N^{(0)} + 2b_{12}^{(0)}\left[\partial_2 b_{11}^{(0)} + b_{12}^{(0)}\kappa_g^{(0)}\right] - b_{11}^{(0)}\left[\kappa_g^{(0)}\kappa_N^{(0)} + \partial_2 b_{12}^{(0)} - \kappa_g^{(0)} b_{11}^{(0)}\right]. \tag{A.5}$$

When $\kappa_N = 0$, Eqs. (A.1) and (A.5) turn into a constraint entirely on the boundary curve because $b_{11}^{(1)}$ drops out. This explains why the inner solutions are singular when $\sim \kappa_N^2 \sim \gamma_\pm = 0$: we can specify $b_{12}^{(0)}$ arbitrarily close to the point $\kappa_N = 0$, but not exactly on the point, this leads to a singularity in the solution which we see in the series solution to Eq. 2.27.

Note that the only isometry of a torus with $\kappa_N = 0$ everywhere on the rigidifying curve is the torus itself, this is easy to see because Eqs. (A.1) and (A.5) completely determine $b_{12}^2 = -\rho^2\ K = 0$ and $b_{11}^2 = -K^1/\kappa_g$, these in turn can be used to determine the full series solution in the variable u^1.

Now we turn our attention to linear deformations, general geometric arguments provide guidance here as well, and can shed light on what is special about surfaces with $\kappa_N = 0$ curves. Imagine a one parameter family of isometries $\mathbf{X}(\epsilon)$, where $\mathbf{X}(0)$ is the starting surface and $\mathbf{X}(\epsilon)$ is the final surface. A linearized isometry can be expressed as $d\mathbf{X}(\epsilon)/d\epsilon\big|_{\epsilon=0}$. For any curve on the surface $\mathbf{X}(\epsilon)$ we can write the following geometric identity

$$\kappa^2(\epsilon) = \kappa_N^2(\epsilon) + \kappa_g^2. \tag{A.6}$$

The linearized version of this identity is $\kappa\ \dot{\kappa} = \kappa_N\ \dot{\kappa_N}$, where a dot over the symbol means a derivative with respect to ϵ. On the rigidifying curve $\kappa_N = 0$, in this case it is obvious that for the linear isometry we have $\kappa = \kappa_g + O(\epsilon^2)$, implying rigid motion of the curve, without change in curvature. It can easily be checked, using Eq. (2.20), that the finite linear isometries to the parabolic torus do indeed satisfy this property.

Yet another check on our solution comes from Eq. A.1. The linearized version of the equation is written as

$$0 = \dot{b}_{11}(0)\ \kappa_N(0) + \dot{\kappa_N}(0)\ b_{11}(0) - 2\dot{b}_{12}(0)\ b_{12}(0). \tag{A.7}$$

On the rigidifying curve of the parabolic torus this gives $\dot{\kappa}_N(0) = 0$, implying that the normal curvature is zero in the linearized isometric deformation. In addition the diverging linear solutions are inconsistent in the linear regime because they have non-zero normal curvature. Yet as we have already seen, $\kappa_N \neq 0$ on the final surface is perfectly well behaved as a nonlinear isometry. Therefore the divergence in the linear solutions is only a reflection of the fact that $\mathbf{X}(\epsilon)$ is not analytic near $\epsilon = 0$.

To conclude this section we demonstrate the non-analyticity of $\mathbf{X}(\epsilon)$ using a simple argument. Eq. (A.6) can be rewritten as

$$\kappa_N(\epsilon) = \pm\sqrt{\kappa^2(\epsilon) - \kappa_g^2}. \tag{A.8}$$

The first order derivative with respect to ϵ diverges at $\epsilon = 0$. Indeed, expanding to first order gives $\kappa_N \approx \pm\sqrt{2\epsilon\ \kappa_g\ \dot{\kappa}(0)}$, which is inconsistent with a first order expansion $\mathbf{X}_0 + \epsilon\ \mathbf{X}_1$ and $\kappa_{N0} + \epsilon\ \kappa_{N1}$, thus explaining the appearance of singular solution in the linear regime.

APPENDIX B

SERIES AND NUMERICAL SOLUTIONS OF ISOMETRIES

The aim of this appendix is to verify our inner solutions against a series and numerical solution of the full isometry Eqs. (2.24 - 2.26). Though we will still neglect the nonlinearities in A_θ and A_s, we can verify explicitly using the approximate inner solutions that these terms are indeed subdominant.

We first check that the series solution of Eq. (2.27) is consistent with the inner approximate solution. Note that Eq. (2.27) is derived from Eqs. (2.24 - 2.26) by eliminating A_s and A_θ and then taking derivatives of the third equation. Therefore any solution of Eqs. (2.24 - 2.26) is a solution of Eq. (2.27), but the converse is not true. In order to make sure that the solutions we find are consistent with the isometry equations, we check that we can use Eqs. (2.24 - 2.26) with $A_z(R) \equiv \epsilon\ \delta$ and $\partial_s A_z(R) \equiv \pm\sqrt{\epsilon\ \gamma}$ to determine the series coefficients of A_s and A_θ. The parameter ϵ is introduced here to control order ϵ terms of the series solution. Thus any solution of Eq. (2.27) is consistent with Eqs. (2.24 - 2.26) only with a particular choice of the integration constant $\tau(\theta)$, which was given to leading order in ϵ back in Eq. (2.44).

In terms $\delta(\theta)$ and $\gamma(\theta)$, the series solution gives

$$\partial_u^2 Y_z(0,\theta) = \frac{\pm\epsilon\ \gamma'_\pm\ \left(\pm\gamma'_\pm - 4\ \sqrt{\epsilon\ \gamma_\pm}\ \delta'_\pm\right) + 4\ \gamma_\pm\ \left(\epsilon^2\ \delta'^2_\pm - 2\ \left(\pm\sqrt{\epsilon\ \gamma_\pm} + \epsilon\ \delta''_\pm\right)\right)}{4\ \gamma_\pm\ \left(\pm\sqrt{\epsilon\ \gamma_\pm} + \epsilon\ \delta''_\pm\right)}, \tag{B.1}$$

However, from the inner solutions we get $\partial_u^2 Y_z(0,\theta) = -2$. To leading order in epsilon, the two expressions agree. This happens at every order in u. We can use boundary

layer theory (see [41]) to determine to which order (in ϵ) the inner solution is valid for every term in the series (in u). This can be done by defining

$$Y_z(u,\theta) \equiv \epsilon\, \mathcal{Y}(\mu,\theta) \qquad \text{and} \qquad \mu \equiv \frac{u}{\epsilon^{1/2}}, \tag{B.2}$$

where $\mathcal{Y}$ as well as its derivatives are O(1) in the interior layer which has width of order $\epsilon^{1/2}$. Using this we can expand $Y_z(u,\theta)$ to get

$$Y_z(u,\theta) \approx \epsilon\, \mathcal{Y} + \epsilon^{1/2}\partial_u \mathcal{Y}\, u + \frac{\partial_u^2 \mathcal{Y}\, u^2}{2} + \frac{\partial_u^3 \mathcal{Y}\, u^3}{6\, \epsilon^{1/2}}. \tag{B.3}$$

Hence we see that the term proportional to u^2 is O(1) with approximation error scaling as $O(\epsilon^{1/2})$. This is indeed what we find in equation (B.1). Using Mathematica we extend Eq. (B.1) to find terms up to order u^{11} in the expansion of $Y_z(u,\theta)$. Fig. (B.1) compares the numerical and series solutions of (2.27) to the approximate solution that we obtain by combining the inner and outer(linear) solutions to form a global approximation.

Finally we use $\gamma_\pm$ and $\delta_\pm$ to find the series expansion of A_θ and A_s, up to integration in the θ direction. We confirm that we can indeed use $\gamma_\pm$ and $\delta_\pm$ to determine the isometry, which implies that solutions of (2.27) that we find are indeed consistent with solutions of (2.24 - 2.26). For example, from the series solution, we have that $\partial_u A_s(0,\theta) = -\epsilon\ R^2\ \gamma_\pm/(8\ a^2)$ which matches what we find from the inner approximate solution. We will not explicitly show the rest of the series solution here for brevity.

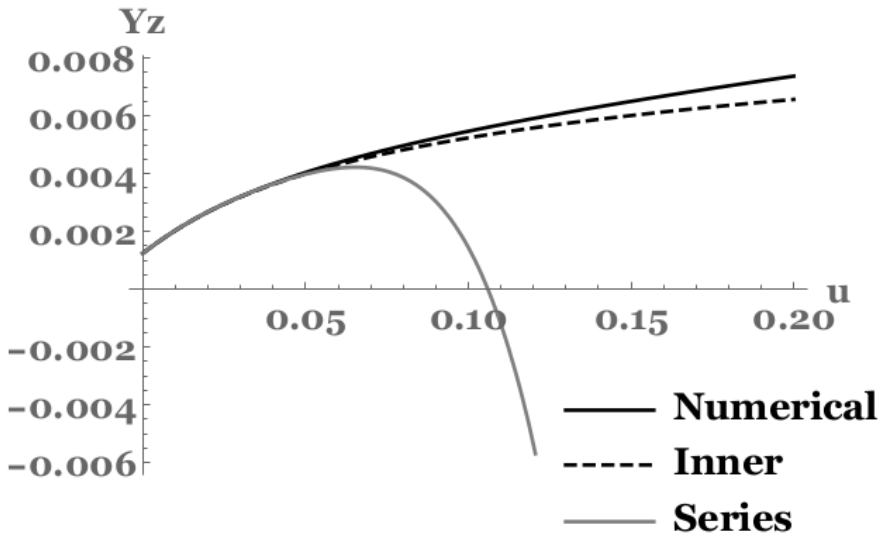

Figure B.1. Comparing the series (up to order u^8) and numerical solutions of Eq. (2.27) to the inner approximation. Here, a = 1, R = 3, $\delta_+ = 0.002\ \cos(2\ \theta)$ and $\gamma_\pm = 0.006 + 0.003\ \cos(2\ \theta)$.

APPENDIX C

GAINING INTUITION FOR THE GROWTH LAW

It is difficult to gain intuition for the terms in Eq. (3.17). To make our life easier we will neglect terms of order $O(\lambda\,\epsilon)$, which is a reasonable approximation if $H\lambda \gg \epsilon$. This approximation leaves only the two leading order stress coupled terms, which is good enough for our current purposes.

The best way to gain intuition is to consider the effect of the various terms on the evolution of special surfaces. Inspired by rod-like *E. coli*, in this chapter we focus mainly on elongating cylindrical shapes. However, we will point out how our analysis could be applied to different shapes such as spherical and flat shapes, which are relevant for other interesting growth process as in blooming lilies and rippling leaves [9, 45].

We start with the simplest term, $\alpha_1 g_{ij}$. For very thin surfaces and in the absence of stretching, we can assume that $\bar{g}_{ij} = g_{ij}$. Therefore with time, the metric will evolve as $g_{ij}(t) = e^{\alpha_1 t} g_{ij}(0)$. Therefore the metric is expanding or contracting exponentially regardless of the initial shape. Furthermore, The linear dimensions of the shell grow exponentially at the rate $\alpha_1/2$.

The next term to consider is $\alpha_2\ b_{ij}$. This term comes from a simple equation of motion $\partial_t \mathbf{X} = -\alpha_2\ \hat{N}$, which is easy to check with the relation $\partial_t g_{ij} = \partial_t \partial_i \mathbf{X} \cdot \partial_j \mathbf{X} + \partial_i \mathbf{X} \cdot \partial_t \partial_j \mathbf{X}$. This evolution is volume minimizing when α_2 is positive. In the case of cylindrical growth, this term will tend to shrink the radius. In the absence of growth at the end caps, which appears to be approximately true for *E. coli* [54], the length will not be affected by this growth term. This gives us a way to fix the radius

during exponential elongation. Specifically, if we set $\alpha_1 = \alpha_2$ we get an exponentially elongating cylinder with fixed radius.

In the case of a growing sphere, setting $\alpha_1 = \alpha_2$ would just stop the growth. On the other hand, the metric of a flat shell would not be affected by this term at all.

Next we consider the term $\beta_1\ (H - H_0)\ g_{ij}$, where we've subtracted H_0 by changing the definition of α_1. This terms couples mean curvature to the rate of growth. It depends on the actual shape and not just on the value of the metric. There is no simple interpretation for $\partial_t \mathbf{X}$ in this case. As we will show, this term with $\beta_1 > 0$ is important for the stability of modes with long wavelength in the longitudinal direction and short wavelength in the azimuthal direction.

Note that the α_2 and β_1 terms are dependent on the global orientation of the normal vector $\hat{N}$, which follows from the definition of the curvature tensor. This was not mentioned in Sec. (3.4.1) as a problem for the invariance of the growth law because we assume the growth process can distinguish between the inside and the outside of the shell. This is not hard to accept in the case of *E. coli* for example. However, for a growing leaf or flower, it might not be possible to distinguish in from out. Therefore, for growing open shells such as leaves, you might set $\alpha_2 = \beta_1 = 0$.

The term $\beta_2\ (H - H_0)\ b_{ij}$ is related to the mean curvature flow. It would result from the motion $\partial_t \mathbf{X} = -\beta_2\ (H - H_0)\ \hat{N}$ and tends to minimize the area when $\beta_2 > 0$. The stabilizing effect of this term is clear. For a cylinder (or a sphere) with radius $a(t)$, we would get $\dot{a} = 0.5\ a_0^2\ \beta_2\ (1/a - 1/a_0)$. The solution to this equation approaches a_0 as $t \to \infty$, behaving like $a \sim e^{-\beta_2\, t}$.

The last geometric growth term we will consider is related to the well known Ricci flow. Namely $\partial_t g_{ij} = -\gamma_1\ g_{ij}$. It is a function of the metric only and we do not need to find the corresponding shape to solve this equation. In order to understand the effect of this term, let's switch to a coordinate system such that the metric can be written in the form $g_{ij} = e^{\rho}\ \delta_{ij}$, this form will be preserved under evolution since the

equation can now be expressed as.

$$\dot{\rho}\, e^{\rho} = -\frac{\gamma_1}{2}\, e^{\rho}\left(-e^{\rho}\nabla^2\rho\right) \implies \dot{\rho} = \frac{\gamma_1\, e^{-\rho}}{2}\nabla^2\rho. \tag{C.1}$$

Notice the resemblance of this equation to the diffusion equation. Indeed, in the vicinity of a cylinder we have $\rho \sim 0$, then to leading order this equation becomes exactly the diffusion equation, which tends to wash out the deformations over time, returning the metric back to the constant flat metric.

Finally we consider the two stress coupling terms. The term $\sigma_1\ \epsilon_{ij}$ will tend to make the target metric $\bar{g}_{ij}$ evolve towards g_{ij} when $\sigma_1 > 0$. In other words, it makes the surface comply with the applied forces, as in the case of *E. coli* [51].

The term $\sigma_2\ \epsilon$ couples the areal strain to the growth rate, ignoring the shear strain. For positive σ_2, and for a given areal strain ϵ, this will make the surface stretch or compress isotropically in a manner proportional to ϵ.

In Sec. (3.5), we will explore how all these terms interact to generate a linearly stable elongating cylinder. But first lets gain more intuition by looking at various toy models of growth processes.

APPENDIX D

MICROSCOPIC TOY MODELS

In this section we will consider various toy (or semi-realistic!) models of growth processes. This will give us valuable insight into how the various terms in Eq. (3.17) might appear and the order of magnitude of their coefficients.

The first model is inspired by the process of swelling polymers films [49, 50]. When polymer films are exposed to a solvent, the solvent molecules will diffuse through the pores in the film and cause swelling of the material. The local rate of swelling can be controlled by different external stimuli such as light and chemical gradients. In the present model we will consider the heterogeneous swelling caused by the curvature of the shells, assuming that only the inner surface is exposed to the solvent.

Since only one side of the shells is exposed then the rate of solvent absorption will depend on the average pore area in the exposed surface. In order to understand the effect of curvature on the exposed pore area we express the exposed surface $\mathbf{X}_{\text{exp}}$ in terms of the mid-surface of the shell in a manner consistent with the Kirchhoff-Love assumptions. Specifically,

$$\mathbf{X}_{\text{exp}} = \mathbf{X} - \frac{\tau}{2}\,\hat{\mathbf{N}}. \tag{D.1}$$

We can use this relation to relate the area element in the exposed surface dA_{exp} to the area element in the mid-surface dA using the relation $dA_{\text{exp}} \equiv \sqrt{g_{\text{exp}}}\; du^1 du^2$. Using Eq. (D.1), we can relate the two metrics using the formula

$$g_{ij}^{\text{exp}} = g_{ij} + \tau\; b_{ij} + \frac{\tau^2}{4} b_i^{\ell}\; b_{\ell j}. \tag{D.2}$$

Using this relation and the identity $\det(A) = \exp[Tr\{\log(A)\}]$, we can find the relation between the two area elements as

$$\frac{dA_{\text{exp}}}{dA} = 1 + \tau H + \frac{\tau^2}{4} K. \tag{D.3}$$

In these systems the growth process is isotropic, meaning that only terms of the form $F_1(H, K)\ g_{ij}$ will contribute. Since curvature changes the area element of the inner surface by the given geometric factor, we conclude that the average exposed pore area will be affected by the same factor. Finally, assuming that the absorption rate in the absence of curvature is given by α_1 we can write the growth law as $\partial_t(dA)/dA_{\text{exp}} = \alpha_1$.

Putting all of this together we get in the curved case that

$$F_1(H, K) = \alpha_1(1 + \tau H + \frac{\tau^2}{4} K). \tag{D.4}$$

Notice that the term H^2 does not appear in this formula due to cancellations in the calculation of the determinant. In addition, the Ricci flow term is suppressed by an additional power of the thickness.

We can also easily imagine how the term $\epsilon\ g_{ij}$ may be generated since ϵ describes to linear order the relative area expansion. The terms proportional to the tensors b_{ij} and ϵ_{ij} are not generated if the growth is isotropic.

Next, we describe toy models where the growth rate of a shell depends on the local concentration of some particle on the surface. This is similar to *E. ecoli* where the local concentration of the protein MreB affects the growth rate of the cell wall [54]. Here we will describe a simple model of passively diffusing particles on the surface. The heterogeneity results from the dependence of the adhesion energy on the local curvature [60, 62]. Another method for achieving heterogeneity would be active particles moving inside or on the surface of the shell [63, 64]

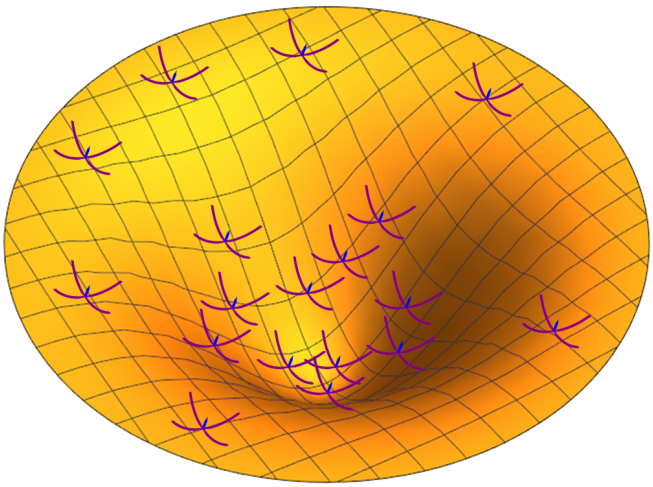

Figure D.1. Shows a "molecule" composed of two perpendicular filaments each with natural curvature $\bar{\kappa}$ and length $\bar{\ell}$ diffusing passively on the surface. The vector shown points to the inside of the closed surface when the filament is attached. The difference in density along the surface is due to biased diffusion based on curvature dependence of adhesion energy

Fig. (D.1) shows a simple diffusing particle composed of two identical orthogonal filaments each with a natural curvature $\bar{\kappa}$ and length $\bar{\ell}$. Assuming that the particles adheres strongly to the surface we can take the realized curvatures of the filaments $(\kappa_{R1}, \kappa_{R2})$ to be determined by the principal curvatures of the surface and the angle θ between the filaments and the principal directions. Explicitly,

$$\kappa_{R1} = \cos(\theta)^2 \, \kappa_1 + \sin(\theta)^2 \, \kappa_2, \tag{D.5}$$

where $\kappa_{1,2}$ are the principal curvatures of the surface. κR_2 follows a similar expression with $\theta \to \pi/2 - \theta$. If we take the bending energy of each filament to be $E_{bi} = Kb \, \bar{\ell} \, (\kappa_{Ri} - \bar{\kappa})^2$, then the total energy in terms of the Gaussian and mean curvatures will be

$$E_b = Kb\,\bar{\ell}\,\bar{\kappa}^2\ \times$$
$$\left(2 - 4\frac{H}{\bar{\kappa}} + \frac{3H^2 - K}{\bar{\kappa}^2} + \frac{H^2 - K}{\bar{\kappa}^2}\cos(4\theta)\right). \tag{D.6}$$

We can easily see that this energy is minimized when $\theta = \pi/4$. The steady state concentration of randomly diffusing particles will be given by a Boltzmann factor $\rho \propto \exp(-\beta\ Eb)$. We also assume, as we have throughout the chapter, that the curvatures of the surface are small compared to the natural curvature of the filament $H << \bar{\kappa}$. Assuming a growth rate proportional to concentration $\partial_t(dA)/dA = C\ \rho$, we get finally that

$$\partial_t \bar{g}_{ij} = \left(\alpha_1 + \beta_1\ \frac{H}{\bar{\kappa}} + \delta_1\ \frac{H^2}{\bar{\kappa}^2} + O\left(\frac{H}{\bar{\kappa}}\right)^3\right)\ g_{ij}, \tag{D.7}$$

were $\alpha_1 \equiv C\ \rho_0$ with ρ_0 being the concentration of the particles when the surface is flat and C being a constant relating the growth rate to the concentration. We also defined $\beta_1 \equiv 4\ \beta\ Kb\,\bar{\ell}\,\bar{\kappa}^2\ \alpha_1$ and $\delta_1 \equiv \beta_1(\beta_1 - \alpha_1)/\alpha_1$.

As mentioned in Sec. (C), the term $H\ g_{ij}$ is dependent on the definition of the normal to the surface. It appears in Eq. (D.7) because we assumed the filament attaches to the inner surface with the arrow pointing opposite to $\hat{N}$. If we relax this assumption or consider an energy like $Eb \sim (\kappa_R^2 - \bar{\kappa}^2)^2$, this term disappears and the leading order terms will be $H^2 g_{ij}$ and $K g_{ij}$.

APPENDIX E

SCALING BEHAVIOR FOR SMALL WAVELENGTHS

In this section, we will study more closely the growth of modes with small wavelengths, namely $q_P \to \infty$. We will gain insight by contrasting the finite and zero thickness cases, starting with the latter.

As can be seen from Eq. (3.28), modes were $q_P \to \infty$ can be stabilized by requiring $\Gamma_2 > 0$. This term ultimately comes from the growth terms Hg_{ij}, Hb_{ij} and Kg_{ij} in Eq. (3.18). Furthermore, we can easily show that as $q_P \to \infty$, these terms scale as

$$H\ g_{zz} \sim H\ b_{zz} \sim K\ g_{zz} \sim q_P^2\ \rho_{mq}. \tag{E.1}$$

We can also easily see, from the isometric solutions given in Eq. (3.25), that $\rho_{mq} \sim G_{\phi\phi}$. This, together with Eq. (E.1) leads to the stabilizing term $q_P^2\ \Gamma_2$ in Eq. (3.28).

Now we can understand qualitatively how finite thickness would change this result. Bending energy suppresses deformations that have wavelengths comparable to thickness, specifically, we get $\rho_{mq} \sim G_{\phi\phi}/q_P^4$. Therefore the stabilizing term proportional to Γ_2 would disappear as $q_P \to \infty$. Next, we examine this case a little more concretely.

First, we minimize the energy with a given metric deformation G_{ij}, and solve for the displacements ρ_{mq}, h_{mq} and ψ_{mq}. we get, for example, that

$$\rho_{mq} \sim O\left(\frac{G_{\phi\phi}}{q_P^4}\right) + O\left(\frac{G_{z\phi}}{q_P^5}\right) + O\left(\frac{G_{zz}}{q_P^6}\right). \tag{E.2}$$

We then plug these solutions back into the growth law and get, for example, that $\partial_t G_{\phi\phi} \propto -\Gamma_2\, G_{\phi\phi}/q_P^2$. Thus we see that $G_{\phi\phi}$ can still be stabilized if $\Gamma_2 > 0$ and in what follows we set $G_{\phi\phi} \to 0$. The other two equations give

$$\partial_t G_{zz} \sim 2\, R\, G_{zz} \quad \text{and} \quad \partial_t G_{z\phi} \sim 2\, R\, \frac{G_{zz}}{q_P}. \tag{E.3}$$

Finally, combining Eqs. (E.3) and (E.1) we discover that

$$\frac{\partial_t \rho_{mq}}{\rho_{mq}} = 4R + O\left(\frac{1}{q_P}\right), \tag{E.4}$$

which validates the result obtained in Eq. (3.30).

BIBLIOGRAPHY

[1] Mound, J. E., Mitrovica, J. X. and Forte, A. M., *The equilibrium form of a rotating earth with an elastic shell*. Geophysical Journal International, 152: 237-241. (2003)

[2] Williams, K. K., Neumann, G. A., Zuber, M. T., *Lunar Mascon Basins: Analysis of Effective Elastic Lithosphere Thickness Using Gravity Anomaly Models*, Abst. of the Lunar and Planetary Sci. Conf., **26**, 1505, (1995)

[3] Billah, K. and Scanlan, R. *"Resonance, Tacoma Narrows Bridge Failure, and Undergraduate Physics Textbooks,"* American Journal of Physics 59 (1991): 118124.

[4] K. Krieger, *Extreme Mechanics: Buckling Down*, Nature (London) **488**, 146 (2012).

[5] Barker, R.J.P. and S.D. Guest. Inflatable Triangulated Cylinders. in IUTAM-IASS Symposium on Deployable Structures: Theory and Applications. 2000. Cambridge, UK.

[6] Zirui Zhai, Yong Wang, Hanqing Jiang. *Origami-inspired, deployable metamaterials*. PNAS, (2018)

[7] O. K. Oyewole, D. Yu, J. Du, J. Asare, D. O. Oyewole, V. C. Anye, A. Fashina, M. G. Zebaze Kana, and W. O. Soboyejo. *Micro-wrinkling and delamination-induced buckling of stretchable electronic structures*. Journal of Applied Physics **117**, 235501 (2015)

[8] Y. Forterre, J. Skotheim, J. Dumais and L. Mahadevan, *How the Venus Flytrap snaps*, Nature, **433**, 421-25, 2005.

[9] H-Y. Liang and L. Mahadevan, *Growth, geometry and mechanics of the blooming lily*, PNAS, **108**, 5516-21, (2011).

[10] Marder M (2003) The shape of the edge of a leaf. Found Physics 33:17431768

[11] H. Liang and L. Mahadevan, *The shape of a long leaf*, PNAS, **106**, 22049, 2009.

[12] Sharon, Eran, Marder Michael, Swinney Harry. (2004). *Leaves, Flowers and Garbage Bags: Making Waves.* American Scientist - AMER SCI. 92. 10.1511/2004.47.932.

[13] Jack Lidmar, Leonid Mirny, and David R. Nelson, *Virus shapes and buckling transitions in spherical shells*, Phys. Rev. E **68**, 051910 (2003).

[14] Andrej Komrlj and David R. Nelson, *Statistical Mechanics of Thin Spherical Shells*, Phys. Rev. X **7**, 011002 (2017).

[15] R. Waugh and E. A. Evans, *Thermoelasticity of Red Blood Cell Membrane*, Biophys. J. **26**, 115 (1979).

[16] A. Kosmrlj, D.R. Nelson, *Response of thermalized ribbons to pulling and bending*, Phys. Rev. B **93** (2016) 125431.

[17] Shikai Deng, Vikas Berry, *Wrinkled, rippled and crumpled graphene: an overview of formation mechanism, electronic properties, and applications*, Materials Today, **19**, Issue 4, Page 197212, (2016).

[18] P. Audoly and Y. Pomeau, *Elasticity and Geometry* (Oxford University Press; 1 edition, 2010).

[19] Manfredo Perdigo do Carmo, *Differential Geometry of Curves and Surfaces* (Prentice-Hall; 1 edition, 1976)

[20] S. Chaïeb, F. Melo, and J.-C. Géminard, Phys. Rev. Lett. **80**, 2354-2357 (1998).

[21] K. Matan, R.B. Williams, T.A. Witten and S.R. Nagel, Phys. Rev. Lett. **88**, 076101 (2002).

[22] Pogorelov, A., *Bendings of Surfaces and Stability of Shells (Translations of Mathematical Monographs, Vol. 72)* (American Mathematical Society, Providence, RI.,1988).

[23] A. Nasto, A. Ajdari, A. Lazarus, A. Vaziri, and P.M. Reis, Soft Matter **9**, 6796-6803 (2013).

[24] A. Vaziri and L. Mahadevan, Proc. Nat. Acad. Sci. **105**, 7913–7918 (2008).

[25] C. D. Santangelo. Soft Matter, **9**, 8246-8251 (2013).

[26] H. Gluck, "Almost all simply connected closed surfaces are rigid." In Geometric topology, pp. 225-239 (Springer, Berlin Heidelberg, 1975).

[27] K. Tenenblat, Proc. Am. Math. Soc. 75, 269 (1979).

[28] B. Audoly, Comptes Rendus de l'Académie des Sciences-Series I-Mathematics, **328**, 313–316 (1999).

[29] B. Audoly and Y. Pomeau, Comptes Rendus Mécanique **330** 425–432 (2002).

[30] N. Bende, A. Evans, S. Innes-Gold, L. Marin, I. Cohen, R. C. Hayward, and C. D. Santangelo Proc. Nat. Acad. Sci. **112**, 11175–11180 (2015)

[31] V. Romero,3, E. Cerda, T. A. Witten and T. Liang, J. Phys. D: Appl. Phys. **41** 132003 (2008)

[32] J. Gemmer and S. C. Venkataramania, Soft Matter, **9**, 8151-8161 (2013)

[33] H.S. Seung and D.R. Nelson, Phys. Rev. A **38**, 1005–1018 (1988).

[34] E. Efrati, E. Sharon, and R. Kupferman, J. Mech. Phys. Sol. **57**, 762–775 (2009).

[35] M. Lewicka and M.R. Pakzad, ESAIM: Control, Optimisation and Calculus of Variations, **17**,1158–1173 (2011).

[36] J. Guven and M.M. Müller, J. Phys. A: Math. Theor. **41**, 055203 (2008).

[37] T C Lubensky, C L Kane, Xiaoming Mao, A Souslov and Kai Sun, Rep. Prog. Phys. 78 (2015) 073901.

[38] J. P. Duncan and J. L. Duncan. Proceedings of the Royal Society of London. Series A, Mathematical and Physical Sciences, **383**, 191-205 (1982).

[39] Marcelo A. Dias, Levi H. Dudte, L. Mahadevan, and Christian D. Santangelo Phys. Rev. Lett. **109**, 114301 (2012).

[40] Alexander E. Lobkovsky Phys. Rev. E **53**, 3750 (1996).

[41] C.M. Bender, S. A. Orszag., *Advanced Mathematical Methods for Scientists and Engineers* (Springer-Verlag New York, 1999).

[42] M.P. Do Carmo, *Differential Geometry of Curves and Surfaces* (Prentice-Hall, 1976).

[43] R.M. Wald , *General Relativity* (University of Chicago Press, 1984).

[44] D'Arcy T. *On growth and form.* Cambridge, University Press, New York, Macmillan. (1945).

[45] M. Marder, E. Sharon, S. Smith and B. Roman. *Theory of edges of leaves.* **62**, 4. (2014)

[46] Tallinen T, Chung J., Rousseau F , Girard N, Lefvre J and Mahadevan L. *On the growth and form of cortical convolutions.* **12**, 588-593. (2016).

[47] Dervaux, J. and Amar, M.B., "Morphogenesis of growing soft tissues," Phys. Rev. Lett. **101**, 068101 (2008).

[48] Castle, T., Cho, Y., Gong, X., Jung, E., Sussman, D.M., Yang, S. and Kamien, R.D., 2014. Making the cut: Lattice kirigami rules. Physical review letters, 113(24), p.245502.

[49] Y. Klein, E. Efrati and E. Sharon. *Shaping of elastic sheets by prescription of non-Euclidean metrics.* Science **315**, 1116-1120 (2007).

[50] Kim J, Hanna JA, Byun M, Santangelo CD, Hayward RC. "Designing responsive buckled surfaces by halftone gel lithography," Science **335**, 1201-1205. (2012).

[51] Amir A., Teeffelen S. *Getting into shape: How do rod-like bacteria control their geometry?* Syst Synth Biol. **8(3)** , 227-235. (2014).

[52] Chang F, Huang KC. *How and why cells grow as rods.* BMC Biol. **12**, 54. (2014).

[53] D. Scheffers and Mariana G. Pinho. *Bacterial Cell Wall Synthesis: New Insights from Localization Studies.* **69(4)**, 585-607. (2005).

[54] T. Ursella, J. Nguyenb , R. D. Mondsa, A. Colavinc, G. Billingsd, N. Ouzounove, Z. Gitaie, J. W. Shaevitzb and K. C. Huang. *Rod-like bacterial shape is maintained by feedback between cell curvature and cytoskeletal localization.* PNAS. **111(11)**, E1025-E1034. (2014).

[55] Amir A, Babaeipour F, McIntosh D, Nelson D, and Jun S. *Bending forces plastically deform growing bacterial cell walls.* PNAS. **111**, 57785783. (2014).

[56] Wong F, Renner LD, zbaykal G, Paulose J, Weibel DB, van Teeffelen S, Amir A. *Mechanical strain sensing implicated in cell shape recovery in Escherichia coli*, Nature Microbiology. **2**, 17115 (2017)

[57] P. Audoly and Y. Pomeau, Elasticity and Geometry (Oxford University Press, Oxford, 2010).

[58] L.D. Landau and E.M. Lifshitz, Theory of Elasticity (Butterworth-Heinemann, Oxford, 1986).

[59] Augustus Love. *A treatise on the mathematical theory of elasticity.* 1, (1892). <hal-01307751>

[60] D. A. Quint, A. Gopinathan, and Gregory M. Grason. *Shape Selection of Surface-Bound Helical Filaments: Biopolymers on Curved Membranes.* Biophys. J. **111(7)** 1575-1585. (2016).

[61] Hannah H Tuson, George K Auer, Lars D Renner, Mariko Hasebe, Carolina Tropini, Max Salick, Wendy C Crone, Ajay Gopinathan, Kerwyn Casey Huang, Douglas B Weibel, *Measuring the stiffness of bacterial cells from growth rates in hydrogels of tunable elasticity*, Mol. Microbiol. **84**, 5, 874-891, (2012)

[62] Wang, Siyuan et al. *Cell Shape Can Mediate the Spatial Organization of the Bacterial Cytoskeleton.* Biophys. J. **104(3)**, 541-552 (2012)

[63] Y. Fily, A. Baskaran, M. F. Hagan. Active Particles on Curved Surfaces. arXiv:1601.00324 [cond-mat.soft].

[64] Hussain S, Wivagg CN, Szwedziak P, Wong F, Schaefer K, Izore T, Renner LD, Sun Y, Bisson Filho AW, Walker S, et al. *MreB Filaments Create Rod Shape By Aligning Along Principal Membrane Curvature.* [Internet]. 2017.

[65] ER Rojas, JA Theriot, KC Huang, *Response of Escherichia coli growth rate to osmotic shock,* PNAS **111** 7807-7812 (2014).

[66] I. R. Booth J. Cairney L. Sutherland C. F. Higgins, *Enteric bacteria and osmotic stress: an integrated homeostatic system*, J. Appl. Microbiol, **65**, 17, (1988).

[67] Hussain S, Wivagg CN, Szwedziak P, Wong F, Schaefer K, Izor T, Renner LD, Holmes MJ, Sun Y, Bisson-Filho AW, et al. MreB filaments align along greatest principal membrane curvature to orient cell wall synthesis. eLife [Internet]. 2018;7 :e32471.